In-Situ Data and Effect Correlation During September 2017 Solar Particle Event

P. Jiggens[1], C. Clavie[2], H. Evans[1], T.P. O'Brien[3], O. Witasse[1], A.L. Mishev[4,5], P. Nieminen[1], E. Daly[1], V. Kalegaev[6], N. Vlasova[6], S. Borisov[7], S. Benck[7], C. Poivey[1], M. Cyamukungu[7], J. Mazur[3], D. Heynderickx[8], I. Sandberg[9], T. Berger[10], I.G. Usoskin,[4,5], M. Paassilta[11], R. Vainio[11], U. Straube[12], D. Müller[1], B. Sanchez-Cano[13], D. Hassler[14], J. Praks[15], P. Niemelä[15], H. Leppinen[16], A. Punkkinen[11], S. Aminalragia-Giamini[9], T. Nagatsuma[17]

Piers Jiggens, piers.jiggens@esa.int

[1]European Space Agency, European Space Research and Technology Centre, Noordwijk, The Netherlands

[2]European Space Agency, European Space Operations Centre, Darmstadt, Germany

[3]The Aerospace Corporation, Chantilly, Virginia, USA

This article has been accepted for publication and undergone full peer review but has not been through the copyediting, typesetting, pagination and proofreading process, which may lead to differences between this version and the Version of Record. Please cite this article as doi: 10.1029/2018SW001936

Abstract. Solar energetic particles are one of the main sources of particle radiation seen in space. In the first part of September 2017 the most active solar period of Cycle 24 produced 4 large X-class flares and a series

[4]Space Climate Research Unit, University of Oulu, Finland

[5]Sodankylä Geophysical Observatory, Finland

[6]Department of Space Science, Institute of Nuclear Physics, Moscow State University, Russia

[7]Université Catholique de Louvain, Center for Space Radiations, Louvain-la-Neuve, Belgium

[8]DH Consultancy, Leuven, Belgium

[9]Space Applications & Research Consultancy, Athens, Greece

[10]German Aerospace Center, Institute of Aerospace Medicine, Köln, Germany

[11]Department of Physics and Astronomy, University of Turku, Finland

[12]European Space Agency, European Astronaut Centre, Köln, Germany

of (interplanetary) coronal mass ejections which gave rise to radiation storms seen over all energies and at the ground by neutron monitors.

This paper presents comprehensive cross-comparisons of in-situ radiation detector data from near-Earth satellites to give an appraisal on the state of present data processing for monitors of such particles. Many of these data sets have been the target of previous cross-calibrations and this event with a hard spectrum provides the opportunity to validate these results. As a result of the excellent agreement found between these data sets and the use of neutron monitor data, this paper also presents an analytical expression for fluence spectrum for the event.

[13]Department of Physics and Astronomy,
University of Leicester, Leicester, UK
[14]Southwest Research Institute, Boulder,
CO, USA
[15]Department of Electronics and
Nanoengineering, Aalto University, Finland
[16]Space Systems Finland Oy, Espoo,
Finland
[17]National Institute of Information and
Communications Technology, Tokyo, Japan

Derived ionising dose values have been computed to show that although there is a significant high-energy component the event was not particularly concerning as regards dose effects in spacecraft electronics. Several sets of spacecraft data illustrating single event effects are presented showing a more significant impact in this regard. Such a hard event can penetrate thick shielding, human dose quantities measured inside the international space station and derived through modelling for aircraft altitudes are also presented. Lastly, simulation results of coronal mass ejection propagation through the heliosphere are presented along with data from Mars-orbiting spacecraft in addition to data from the Mars surface.

Keypoints:

- Comparison of solar energetic particle fluxes, doses and other effect quantities in events of September 2017
- Analysis of the sources of differences in fluxes observed by instruments at Earth and also at Mars
- Presentation of complete fluence spectrum for the solar particle event as seen at Earth using space- and ground-based data

1. Introduction

Radiation storms, known as Solar Particle Events (SPEs), are characterised by large enhancements of particle radiation fluxes from the Sun, including protons, electrons and heavier particles, which may pose a hazard for spacecraft operations and humans where (physical and magnetic) shielding is limited [*Malandraki and Crosby*, 2018]. Since 2014 an international working group has convened at regular intervals to discuss the Harmonisation of Solar Energetic Particles (SEP) Data Calibrations (HSDC). The ultimate goal is the construction of reference data sets with well-defined uncertainties derived from the measurement process and data post-processing.

Comparisons and cross-calibration of in-situ radiation data are of critical importance for improving the accuracy of specifications of the space environment, space weather predictions and the outputs of relative scientific studies. For scientists working on these topics the issues pertaining to data processing are often not the subject of their work. However, testing scientific hypotheses can benefit strongly from carefully processed radiation instrument data with identification of caveats and removal of measurement artefacts. This area of research bridges the gap between instrument developers, who often possess essential information on the characteristic features of instruments, and radiation environment specialists, who understand the sensitivity of models to instrument response.

SPEs provide an excellent opportunity to compare the response of different instruments in space due to the shallow spatial gradients (variation in fluxes changing little as a function of distance) seen during such events. This is: the incident radiation environment can be considered identical for spacecraft across the full range of Earth orbits before

geomagnetic shielding is taken into account. After the initial onset, SPEs also provide an environment which is relatively isotropic [*Rodriguez et al.*, 2014] such that for the majority of the time the impact of the instrument viewing direction can be ignored (other than to consider the access of particles within the magnetosphere).

The aim of this paper is to bring together a wide range of available in-situ radiation monitor data and to compare time series and spectra during the large radiation storms observed during the first half of September 2017 as a test to understand the uncertainties between instruments. This allows the derivation of a fluence spectrum ranging in energy from 10 keV to 1 GeV which can be applied in future studies. The effect of the SPE is investigated in terms of component and radiation quantities related to human exposure, and Single Event Effect (SEE) rates for Earth-orbiting spacecraft. Finally, the event at Mars is investigated.

2. Events on the Sun

Some of the most significant activity of solar cycle 24 occurred in early September 2017. On 1st September, the sunspot Active Region (AR) 12674 containing two massive sunspots appeared on the Eastern limb of the solar disc. Below, a small sunspot was embedded in AR 12673. By 4th September AR 12673 had developed into a much more magnetically complex configuration than AR 12674, and as the Sun rotated and the region faced Earth, it released three M-class solar flares: An M1.3 flare peaking at 05:49 UTC, an M1.5 flare peaking at 15:30 UTC and an M5.5 flare peaking at 20:33 UTC. However, AR 12673 was still developing. Figure 1 shows the two clusters of sunspots and active regions as viewed by the Helioseismic and Magnetic Imager (HMI) instrument on-board NASA Solar Dynamics Observatory (SDO) on 6th September.

The largest eruption, an X9.3 flare with a peak X-ray flux at approximately 12:02 UTC on 6th September 2017, was also the largest solar X-ray flare seen for 12 years. X-class solar flares (fluxes of X-rays with wavelengths between 1 and 8 Å greater than 10^{-4} W/m^2) are the highest category of solar flare and these events show that although the Sun was approaching the quiet period in its (approximately 11-year) cycle, significant eruptions may still occur. Figure 2 shows this flare as observed by the Atmospheric Imaging Assembly (AIA) instrument on-board SDO at two wavelengths (171 & 304 Å). The flare occurred at a solar longitude of approximately 35 degrees West. This gives a reasonably good magnetic connectivity to the Earth but did not provoke a very large radiation storm at higher energies (> 100 MeV).

There was a second huge (> X5) eruption; an X8.2 flare which peaked at 16:06 UTC on Sunday 10th September 2017. These eruptions were accompanied by fast expulsions of coronal plasma known as Coronal Mass Ejection (CMEs) and their associated interplanetary shocks which are capable of accelerating particles to very high energies resulting in large, gradual SPEs [*Reames*, 1999]. These events were observed by various space observatories. Figure 3 (a) shows an EUV difference image (a subtraction of the pixels in one frame from those in the following frame) shortly after the onset of the second X-class flare which appears to show the lift-off of the CME from the solar limb; the ejecta appearing as a horizontal tear-drop to the right of the image. A multi-wavelength composite image is shown in Figure 3 (b) indicating the location of the active region. Figure 3 (c) shows images from the LASCO C2 and C3 coronagraphs on-board the ESA/NASA SOHO spacecraft with a composite high contrast EUV image to highlight the flaring on the solar disc. The CME drives a strong shock ahead of it (with an initial launch speed of 2600

km/s [*Guo et al.*, 2018]) which accelerates particles up to GeV energies. The substantial increase of transient tracks and spots seen on the coronagraph images after the flare result from the high-energy particles hitting the imaging instruments' detectors, an example of this is given with the wider field-of-view difference image in Figure 3 (d).

The origin of this second (> X5) flare was the same solar active region AR 12673, which had by this time transited to beyond the Western limb of the Sun (see Figure 3 (top right)). A description of the evolution of AR 12673 is given by *Redmon et al.* [2018]. The magnetic connectivity was similar to the earlier solar event but on this occasion the CME-driven shock resulted in a large radiation storm which was the largest of solar cycle 24 at the highest energies [*Kataoka et al.*, 2018]. This may arise from the preceding activity with the multiple eruptions providing an energetic particle seed population that was subsequently accelerated in the event of 10th September [*Schwadron et al.*, 2018]. This demonstrates the complexity of forecasting radiation storms from solar activity. X-ray signatures show a correlation with radiation storm intensities but with a great deal of variability. CME characteristics (especially speed) show a better agreement but still with a significant scatter of particle radiation intensities. Solar connectivity is increasingly important at higher energies due to the rapidly decreasing shock strength associated with the CME and the related reduction in capacity for accelerating particles to the highest energies [*Smart and Shea*, 1985]. Other factors, such as the expansion and resulting width of the CME, also play a crucial part.

Figures 1, 2 and 3 have been produced using the latest version of the JHelioviewer software [*Müller et al.*, 2017], part of the open source ESA/NASA Helioviewer Project. The evolution of AR 12673 and the shearing motion between the sunspots with opposing

magnetic polarities which resulted in it being the most actively flaring region of Cycle 24 has been studied by various authors including *Sun and Norton* [2017] and *Yan et al.* [2018].

3. In-Situ Radiation Data

The National Oceanic and Atmospheric Administration (NOAA) in the US monitors solar activity and the in-situ radiation environment at Geosynchronous Earth Orbit (GEO) through its GOES satellites which are usually operating in pairs with one satellite over the West coast and one over the East coast of the United States. The primary GOES satellite during this period was GOES-15 which observes the proton radiation environment at medium energies (nominally between 1 and several hundred MeV) with the Energetic Proton, Electron and Alpha Detector (EPEAD) and high energies (above 350 MeV) using the High Energy Proton and Alpha Detector (HEPAD) as well as solar X-rays using the X-ray Sensor (XRS). Figure 4 shows the X-ray fluxes observed over the period related to the SPE and the proton fluxes observed over the 9 energy channels for detectors on the same spacecraft but one facing West (colored lines) and the other East (grey lines). This includes the two > X5 flares on 6th and 10th September and an X1.3 flare on 7th September. However, an X2.2 flare reported by other authors (e.g. *Redmon et al.* [2018]) earlier on 6th September is missing from the record due to a 50-minute data gap resulting from an eclipse period of the GOES-15 satellite. The vertical grid lines are chosen to match the flare peak intensities for the two > X5 flares. The nominal energy lower and upper bin limits (E_l and E_u) are shown in Table 1. Positively charged particles with gyrocentres outside the Earth's magnetosphere can more easily access a detector facing in the West direction [*Rodriguez et al.*, 2010]. This effect is most apparent at lower energies where

particles have a lower magnetic rigidity and are therefore more easily deflected. Therefore for the remainder of this study only the West-facing GOES detectors are used.

Sandberg et al. [2014] derived accurate effective mean particle energies for the GOES/EPEAD energy bins for channels 2 - 7. The application of this method applied to GOES-11/EPEAD data is shown in Table 1. Note that there are only small differences between these E_{eff} values and those derived for GOES-8 documented by *Sandberg et al.* [2014]. The resulting effective energies derived for GOES-11/EPEAD through this cross-calibration process have been applied (unaltered) to GOES-15 and the result is shown in Figure 5. The updated spectrum is markedly smoother than using the geometric energy bins. Work by [*Rodriguez et al.*, 2017] has demonstrated the excellent agreement of integral fluxes derived using the effective energies with those measured by instruments on the IMP-8 and STEREO spacecraft. Here we show the spectral comparison to data from the RPS instrument on the Radiation Belt Storm Probes (or Van Allen Probes). The free-space isotropic average flux for RPS has been inferred for particles with gyrocenters at an L value greater than 6 by exploiting the spin of the RBSP spacecraft and the East-West effect to exclude particles approaching from lower altitudes. This has been scaled to the duration of the enhancement starting at 16:10 on 10th September and ending at 16:00 on 14th September to estimate a fluence. The spectra shows good agreement with the spectra from GOES based on effective energies. From hereon all GOES fluxes and spectra are based on the effective energies of *Sandberg et al.* [2014].

3.1. Comparison of in-situ measurements

The high-energy proton increase from the 10th September event was also promptly observed by a number of radiation monitoring instruments on European and Russian

spacecraft including INTEGRAL (INTErnational Gamma-Ray Astrophysics Laboratory), XMM-Newton, Proba-1, Proba-V, Giove-A, AlphaSat, Galileosat-15, Electro-L2 and Meteor-M2. Figures 6 and 7 show comparison of time series data from GOES with the INTEGRAL Radiation Environment Monitor (IREM) and the Standard Radiation Environment Monitor (SREM) on Proba-1 respectively. INTEGRAL (Figure 6) is in an eccentric inclined orbit with perigee of $\sim$ 10000 km and apogee of $\sim$ 150000 km (the inclination varies over the mission but was 49.5° in at the time of the SPE). The data gap observed during the first part of the event is due to removed data during the spacecraft perigee pass where SEPs are partially shielded and the detector sees trapped particles. Proba-1 (Figure 7)is in a sun-synchronous low-Earth orbit at an altitude of $\sim$ 600 km where SEPs are only detectable at higher latitudes and so the data appears more sparse but regular [*Sandberg et al.*, 2012]. All fluxes have been interpolated point-by-point using a power law to give fluxes at the same energies - those applied in ESA's SEPEM (Solar Energetic Particle Environment Modelling) system [*Crosby et al.*, 2015]. The agreement for all IREM with GOES/EPEAD is excellent, with the two generally within $\sim$ 20% of one another. For the SREM instrument on Proba-1, the agreement remains excellent for the lower energy channels but diverges at the highest energy of 244.2 MeV. Figure 7 also shows possible contamination from higher energy protons in the lower energy channels on GOES/EPEAD peaking at 18:45 UTC on 10th September just after the flare when the highest energy particle are arriving. This peak is not seen in either the SREM or IREM data sets.

ESA's Proba-V satellite, operating in a Sun-synchronous low-Earth orbit with an altitude of $\sim$ 820 km, carries the EPT (Energetic Particle Telescope) instrument [*Cya-*

mukungu et al., 2014]. Energetic proton time series derived from EPT are depicted in Figure 8 for the parts of the Proba-V orbit most exposed to interplanetary space, i.e. over the Earth's polar regions where the geomagnetic shielding is at its weakest. The Russian Electro-L2 satellite, like GOES, is operating at GEO although the Electro-L2/SKL (Solar cosmic ray spectrometer) detector is South-facing unlike the GOES/EPEAD detector which is West-facing. Data from Electro-L2 and GOES/EPEAD are also plotted in Figure 8. GOES/EPEAD and Proba-V/EPT data have been interpolated to the Electro-L2 channel mean energies. These mean energies have been estimated from the Electro-L2 nominal bin limits by using the shape of the GOES fluence spectra from Figure 4 assuming a flat response from particles of all energies over the energy bin (a step function). At the higher Electro-L2 energy of 20-40 MeV the agreement is excellent, except in the first part of the event, indicating that the derived effective energy of 26.1 MeV is appropriate. The difference in the first part may be due to a greater portion of the flux coming from higher energies during onset when the spectra is harder or a contamination effect. At the lower Electro-L2 energy of 9-20 MeV the agreement using the derived effective energy of 12.8 MeV is not as good, indicating that the Electro-L2 detector has a greater response to lower energy particles. An interpolation of GOES data to 10 MeV shows better agreement for this channel. The comparison of GOES/EPEAD and EPT is excellent at both energies and here again the EPT flux only deviated significantly at the onset of the event likely due to contamination in the GOES/EPEAD data mentioned previously.

Figure 9 shows the differential proton fluence spectra of GOES/EPEAD and RBSP/RPS alongside that of the IREM, SREM and Electro-L2 instruments. To complete the fluence spectra the GOES/EPEAD data have been interpolated to the IREM, SREM, EPT and

Electro-L2 energies and a histogram of the flux contribution as a function of time has been calculated. The fluences from the other instruments have been multiplied by a factor derived from the GOES/EPEAD flux histograms to account for the time duration where observing the SPE was not possible. For example, the IREM measurements were usable 58.8% of the time duration of the SPE as shown in Figure 6. These summed time intervals included 69.4% of the fluence in the GOES/EPEAD data interpolated to the same energy. However, the same time intervals only included 37.4% of the fluence seen by GOES/EPEAD at the highest IREM energy channel. Factors were derived for all native energies and used to scale IREM, SREM, EPT and Electro-L2 for all energies to give a consistent picture of the agreement in terms of fluence accumulated over the SPE. The deviations indicated in the Figures 6, 7 and 8 are also visible in Figure 9. For the derived effective energies, the Electro-L2 data have very good agreement with the other data sets at the higher energy of 26.1 MeV but a reduction in the derived effective energy from 12.8 to approximately 10 MeV would be appropriate for the lower energy channel as hinted at in the time series analysis shown in Figure 8.

Data have been analysed from the Space Environment Data Acquisition (SEDA) instrument on-board the Japanese weather satellite Himawari-8 [*Nagatsuma et al.*, 2017] which is in a Geosynchronous Earth Orbit (GEO) at $140.7^{/circ}$ East. There are 8 separate Proton Telescopes (PTs) included as part of the SEDA instrument. The proton fluxes were derived using the 'Bow-Tie' unfolding method [*Van Allen et al.*, 1974]. The fluxes shown in Figure 10 are calculated for the effective energy values of the PTs (20-70 MeV) treating each channel independently. The SEDA data, integrated over 5-minute intervals from its native 10-second time resolution, is compared to GOES/EPEAD data interpo-

lated to SEDA/PT energies. The PT data may be contaminated by electrons and further work is needed to address these issues in the data processing. Similar to the second GOES detector but unlike the other data shown in this article the SEDA detector is East-facing. This can account for the suppression of SEDA/PT fluxes with respect to the West-facing GOES-15/EPEAD fluxes and it is noticeable that at several times during the SPE there is excellent agreement most likely due to a compression of the Earth's magnetosphere and changes in the ring current during the geomagnetic storm allowing greater access for particles at these energies. The drop-outs, especially the one on 13th-14th September, match closely the behaviour of the GOES-15 East-facing detector shown in Figure 4. The SEDA/PT data is therefore most suitable for studies of particles with gyro-centres inside the Earth's magnetosphere and the East-West effect during SPEs such as explored by *Rodriguez et al.* [2010].

To extend the outlook one can look also at electron fluxes during the event. The SURF sensor of SEDA instrument, is based on the heritage of the SURF, CREDO and Merlin [*Ryden et al.*, 2015] and permits the indirect measurements of electron fluxes as shown in Figure 11. SURF is a stack of charge collecting plates optimized to measure internal surface charging currents resulting from energetic electron fluxes and is characterized by negligible contamination by protons during SPEs. It is important to note that these electron fluxes are not solar electrons but rather trapped electrons which vary as a result of geomagnetic disturbances.

Lower energy ion data (dominated by protons) are available from the EPAM instrument on-board NASA's Advanced Composition Explorer (ACE). The time series for the period of interest is shown in Figure 12 along with the GOES data interpolated to the SEPEM

reference energies. This figure shows that whilst the powerful shock of the CME launched from the Sun's Western limb generates peaking values of high energy particles after ~ 6 hours, the lower energy particles peak 2 days later when the limb of the expanded CME and shock pass the Earth. Data from Figure 12 were used to derive integral fluxes for energies from > 1 MeV to > 260 MeV and these integral fluxes are presented in Figure 13. The SKL instrument on-board the Russian Meteor-M2 satellite measures particles in energies from 1-100 MeV and 30-260 MeV from a low-Earth orbit with flux time series labelled S and N denoting the measurements averaged across the polar caps in the Southern and Northern hemispheres respectively. By adding the integral particle fluxes from GOES for energies above the higher energy bin limits of these channels the fluxes can be compared to integral fluxes derived from ACE/EPAM and GOES/EPS measurements shown in Figure 12. Figure 13 shows that the Meteor-M2 fluxes at > 1 MeV have a good agreement with the shape of the ACE-GOES composite but are on average $\sim 30\%$ higher. The Meteor-M2 fluxes at > 30 MeV by contrast are a factor of ~ 3 lower than the same energy for the GOES data (matching much better the > 50 MeV channel) so this would warrant further investigation.

3.2. Ground Level Enhancement

When the particle radiation is sufficiently energetic, it reaches Earth's atmosphere and induces the production of secondary neutrons which are detected by Neutron Monitors (NMs) at the Earth's surface. This is known as a Ground Level Enhancement (GLE). This was the case for the radiation enhancement produced by the solar events of 10th September which resulted in GLE72 [*Kurt et al.*, 2018; *Redmon et al.*, 2018]. An interesting feature of GLE72 was that the energetic protons arrived very quickly following the X-ray flare,

implying a very good magnetic field connection to the site. The solar rotation means that good connectivity is usually between 45 and 60 degrees in solar longitude West of the central meridian. However, this flare occurred close to the Sun's limb ($\sim$ 90 degrees West) implying rapid angular expansion of the associated CME low in the solar corona. We have utilised NM data for 3 hours from 16:10 until 19:10 on 10th September to estimate the high energy component of the SPE fluence. Due to the propagation speed of the very high energy particles, which produce secondaries detectable by NMs, and the rapid reduction in shock strength, limiting its capability to accelerate such particles, it is reasonable to assume that the bulk of protons above 1 GeV arrived in this time window. To complete the energy spectrum for the event, we use fitted spectra for 20 time stamps over the 3-hour period for energies ranging from 450 MeV to 1 GeV.

Figure 14 shows the fluence spectrum for the 10th September SPE with the ACE/EPAM data for the lowest energy protons ($<$ 5 MeV), the corrected GOES data for the mid-energy protons ($>$ 5 MeV and $<$ 300 MeV) and the NM data for high energy protons ($>$ $450MeV$). The plot also includes the RBSP/RPS data for comparison. It should be noted that these NM data require the subtraction of the background Galactic Cosmic Ray (GCR) flux which remains visible in the highest energies of the RPS instrument ($>$ 400 MeV). Figure 14 also shows a spectral fit made to the data points shown excluding the lowest energy channel from ACE/EPAM applying a double power law fit with exponential rollover at intermediate energies [*Band et al.*, 1993; *Mewaldt et al.*, 2005; *Tylka and Dietrich*, 2009] to the differential fluence spectrum. The function is given by:

$$\mathrm{d}\phi/\mathrm{d}R = 2.05 \times 10^{10} \cdot R^{-0.893}\exp(-R/0.0891) \text{ for } R \leq 0.525$$

$$\mathrm{d}\phi/\mathrm{d}R = 1.26 \times 10^{6} \cdot R^{-6.79} \text{ for } R \geq 0.525$$

where R (in GV) is the particle rigidity (momentum divided by charge) and ϕ is the SPE fluence or peak flux.

4. Effects of the SPE

4.1. Effects on Spacecraft

Figure 15 shows an estimate of the cumulative ionizing radiation dose from the event as compared to past solar events as seen by the US NOAA GOES and SMS spacecraft in geostationary orbit. These data are taken from the background-subtracted SEPEM reference data set version 2.1. These data show that the event was large but not exceptional and that the dose behind nominal shielding was relatively low ($\sim$ 200 rads at 4 mm Al shielding) compared with the largest SPE (the so-called Bastille Day event of July 2000) which was almost an order of magnitude larger. In Earth orbits, where doses are dominated by the radiation belts, an SPE of this size would not severely impact components from an ionizing dose perspective. Only the largest SPEs provide a significant delta to the radiation belt dose expected over a mission lifetime and the contribution of this SPE would certainly be covered within usual spacecraft specifications. At a higher shielding thickness (20 mm Al) the SPE dose is the 12th largest but the total dose seen in such strongly shielded environments are low and the largest event (that of October 1989) is a factor of $\sim$ 7 higher.

Several anomalies occurred on different spacecraft in Earth orbits as a direct impact of the solar activity on 10th September (Figures 16, 17 and 18). At 17:18 the XMM-Newton satellite temporarily lost its guide star. The lost guide star was recovered again at 18:50 that day. The Swarm satellites, operating in low Earth orbit at 450 km and 530 km, witnessed an EDAC (Error Detection And Correction) Code-Area anomaly on

the ACCelerometer (ACC) payload instrument on-board Swarm-C at 22:19 UTC. This anomaly is an EDAC correction problem caused by a corrupted RAM memory which holds the software code. It is reoccurring but is identified by the operations team as space weather related and the sudden rise in proton flux is the most probably cause of increased Single Event Upset (SEU) rate which led to the anomaly. On 11th September at 03:54 UTC, another anomaly occurred on-board Swarm-B: The Vector Field Magnetometer (VFM) generation time of the science packets was frozen, leading to loss of science data. The science packets were received but with a wrong packet generation time.

A technology demonstration payload flying on the AlphaSat platform in Geostationary Earth Orbit carries a memory test board including SEU and Single Event Latch-up (SEL) experiments. Figure 16 shows the upset rate for 12 memories flying on this test board as well as detail on two of the memories showing that the period included a higher rate of Single Bit Upsets (SBUs) and Multiple Bit Upsets (MBUs) well correlated with the peak in the SPE on 11th September. The total number of bit errors do not distinguish between single bit flips and multiple bit flips originating from the same particle strike (or event). The SBU and MBU rates include only events resulting from a single incident particle hit.

Also on September 11th an anomaly on board Cluster-4, operating in a highly elliptical Earth orbit, was reported on data packets downlinked at 15:30. While dumping the Solid State Recorder (SSR) data a continuous alarm was reported that VC2 Frame gaps occurred. The anomaly was identified as space weather related by checking the Bit Error Rate (BER) of the SSR. The daily BER for all 4 Cluster spacecraft is shown in Figure 17. On September 11th (doy 254) the BER suddenly jumps an order of magnitude for Cluster-4 indicating the impact of the SPE on the SSR. The BERs for the SSR on Cluster-2 and

Cluster-3 are shown as zero for 11th September but are much higher on 12th September. This is inconsistent with the data from Cluster-1 and Cluster-4 and the Alphasat/MTB data shown in Figure 16. It is therefore likely a result of delay in correction of the bits or downlinking the BER to ground.

The impact of the SPE was also responsible for effects on the Aalto-1 spacecraft operating in Low Earth Sun-Synchronous Orbit at an altitude of 550 km and an inclination of 97.46 degrees. Aalto-1 [*Kestilä et al.*, 2013] is a three-unit CubeSat which was launched on 23 June 2017. The on-board computer (OBC) has been in constant operation and consists of two (cold-redundant) Atmel AT91RM9200 processors running Linux. However, during the September 2017 solar storms a large number of radiation-related reboots has occurred. Most likely, this is related to very energetic protons interacting with electronics. Figure 18 depicts the boot-ups of the system since the beginning of the mission and shows the relation to the reboot times to proton increases.

4.2. Doses Levels at ISS

The September 2017 SPE was the first event since May 2012 also observed with radiation detectors inside the International Space Station (ISS). An example of data from the DOSIS 3D DOSTEL instrument [*Berger et al.*, 2017], which is placed below the EPM (European Physiology Modules) rack in the European Columbus Laboratory of the ISS, is shown in Figure 19. Figure 19 provides the GOES-15 proton flux for energies > 100 MeV and the absorbed dose rate (in Si) measured with the DOSIS 3D DOSTEL instruments for 10th to 13th September 2017. Even though the event started at 16:04 UTC on 10th September, the ISS only reached lower geomagnetic cut offs (Rc), allowing the solar energetic protons to reach ISS, at around 04:00 on 11th September 2017 with the main peak of the event

following at 07:30 UTC on 11th September. Higher dose rates were still observed on 12th September 2017 at low Rc values. This is in agreement with GEANT4 calculations performed by [*Matthiä et al.*, 2018] for the event [*Berger et al.*, 2018]. The additional dose due to the event inside the ISS accounts for around 67.8 μGy in Si [*Berger et al.*, 2018].

4.3. Dose Levels at Aircraft Altitudes

On the basis of derived spectra using neutron monitor data and employing a recent model [*Mishev and Usoskin*, 2015], we computed the effective dose rate during the event at several commercial flight altitudes, the details are given in this volume [*Mishev and Usoskin*, This issue]. An example of the effective dose rate distribution at an altitude of 40000 feet (12.2 km) above sea level during the peak intensity of GLE 72 is given in Figure 20. As expected the effective dose rate is at maximum at polar and sub-polar regions, where the cut-off rigidity is marginal. More details on GLE72 can be found in *Kataoka et al.* [2018].

5. The Event at Mars

The SPE sparked on September 10th had a clear impact on measurements on the Martian surface and on measurements made by spacecraft orbiting Mars. As the AR 12673 was on the Western limb of the Sun at this time and Mars was located behind the Sun at roughly 155 degrees, the SPE was an Eastern event as seen from a spacecraft at Mars (Figure 21 panel (a)). Figure 21 panel (b) displays a WSA-ENLIL+CONE simulation of the solar wind and CME propagation within 3 AU. The CME reached Mars around 13th September. The flare and the SEP are seen in the Mars Odyssey HEND (High Energy Neutron Detector), and Mars Express ASPERA3 background and

housekeeping data (panel c), in the period 10th - 15th September. The HEND data comes from the scintillator block which is used in coincidence to correct the background induced in the other sensors (proportional counter detectors) due to secondary neutrons induced in the instrument rather than secondary particles emitted from the Martian atmosphere. However, the signal is a strong indirect measure of the incident SEP population during particle events.

The Mars Atmosphere and Volatile Evolution Mission (MAVEN) and the Mars Science Laboratory-Radiation Assessment Detector (MSL-RAD) [*Hassler et al.*, 2012] on the Curiosity rover also observed this space weather event, as shown in Figure 22. Panel (a) displays protons in the energy range 15-220 MeV detected by MAVEN during the same period. At the surface, the event was detected by the Radiation Assessment Detector (MSL-RAD) [*Hassler et al.*, 2018; *Lee et al.*, 2018], see Panel (b). This was the first GLE observed on two planets simultaneously. The absorbed dose measured with the MSL-RAD E detector shows a statistically significant increase in dose rate around 19:50 UTC on 10th September. The total dose measured with the MSL-RAD E detectors amounts to 369 μGy for the event [*Zeitlin et al.*, 2018]. A Forbush decrease can be seen on 13th September, indicating the arrival of the CME. This SPE is one of the largest observed by Mars Express since 2004 and the largest observed by MSL-RAD on the surface of Mars since its landing in March 2012.

6. Conclusions

In-situ observations have been presented of a large Solar Particle Event (SPE) with onset first observed at Earth shortly after 16:15 on 10th September 2017. Assuming a solar wind velocity of 400 km.s^{-1}, this is consistent with injection of 150 MeV protons at

the Sun just before 16:00 as 150 MeV protons should take 18.5 minutes to propagate from the solar surface assuming a static Archimedean (or Parker) spiral in the ecliptic plane (see, for example, [*Malandraki and Crosby*, 2018]):

$$z(r) = \frac{a}{2}\left[\frac{r}{a}\sqrt{1+\frac{r^2}{a^2}} + \ln\left(\frac{r}{a}+\sqrt{1+\frac{r^2}{a^2}}\right)\right]$$

where z is the distance along the Interplanetary Magnetic Field (IMF) line, r is the radial distance from the Sun and $a = u/\Omega$ where u is the (constant) solar wind speed and Ω is the angular speed of solar rotation. This arrival time coincides with the peak of an X8.2-class solar flare which was observed at 16:06 but therefore occurred at approximately 15:58 due to the time is takes light to travel 1 AU. The onset of the flare was observed at 15:40 and by the time of the X-ray peak the CME lift-off was observable in EUV images from SDO. By 16:15 the associated CME was detectable in coronagraph images from SOHO. As the solar event occurred at (or beyond) the Western limb of the solar disk the detection of particle radiation at the same time as the CME becoming visible in the coronagraph indicates a rapid lateral expansion of the shock. This is consistent with the detected EUV wave signature from GOES-16/SUVI as reported by *Seaton and Darnel* [2018].

The primary goal of this work was take advantage of the SPE which presents approximately equal fluxes at all near-Earth locations prior to shielding by the Earth's magnetosphere, to demonstrate that good agreement is found between space-based particle radiation instrumentation data. Particularly good agreement is shown between the re-calibrated data from GOES-15/EPEAD and INTEGRAL/IREM with differences generally below 20% where international collaborations have led to the development of processing chains for instrument cross-calibration [*Sandberg et al.*, 2014; *Rodriguez et al.*,

2017]. In addition data from Proba-1/SREM, Proba-V/EPT, Electro-L2, Meteor-M2 and Himawari-8/SEDA show good agreement but also some differences indicating avenues for further research. Based on their propagation speed, lower energy protons (<10 MeV) should arrive at Earth approximately 1 hour later than the 150 MeV protons. However, onset appears much earlier than this in lower energy radiation monitor channels (most apparent in the GOES-15/EPEAD data but likely present in other instruments) likely due to sensitivity of particles of much higher energy. Instrument responses are not pure boxcar functions and bin limits are estimated from the responses based on assumed spectral forms. In the absence of low energy particles this assumption breaks down. The high energies to which the particles were able to be accelerated by the CME resulted in increases in fluxes of secondary neutrons on the ground measured by neutron monitors. This combination of space-based and ground-based measurements has allowed for the presentation of a fluence spectrum for the event which can be useful for future studies. This spectrum is consistent with the science-class flux data derived from measurements from the RPS instrument on-board the RBSP satellites.

It is expected that this study shall give users of radiation monitor data increased confidence and understanding regarding its accuracy. It should be noted that the measurements at low altitude (Proba-1, Proba-V, Meteor-M2 and ISS) are influenced by the geomagnetic field in important ways. One is geomagnetic shielding, where fluxes are increasingly attenuated with decreasing latitude. Although the Proba-1/SREM and Proba-V/EPT data presented here have been selected for only the higher, least affected, latitudes, the full data sets will allow this effect to be studied in detail and compared with model predictions in future work. The other effect is on the angular distribution of the fluxes. The

strong field at low altitudes gives rise to important directional effects that will also be the subject of further investigations. *O'Brien et al.* [This issue] have investigated the effect of this event on the geomagnetic cut-offs observed for satellites near Earth by use of the RPS data.

The Earth measurements shown in Figure 4 show a peak in all energy channels occurring in the first part of the event. The reason for this is most likely that, as shown in Figure 21 (a), the shock, propagating in the upward direction, is initially relatively well connected magnetically to the Earth. After a short period of lateral expansion of the CME and the formation of its associated shock, the particles could access the interplanetary magnetic field line connected to the Earth. By the time the shock is passing a solar radial distance of 1 AU (shown in Figure 21 (b)) the shock front is very poorly connected to the Earth so particle fluxes across all channels are greatly reduced. The HIMAWARI/SEDA/SURF detector measuring electrons shows no immediate correlation with the proton fluxes as the electrons measured are trapped and the instrument does not suffer from contamination issues. Nonetheless arrival of CMEs and SIRs does impact these populations sometimes resulting in reductions in radiation belt fluxes and at other times enhancements. More details on electron fluxes and how they were affected during this storm can be found in *Redmon et al.* [2018].

The SPE was also observed by MAVEN, Mars Odyssey and MSL-RAD at Mars. If Earth and Mars were both connected to the particle source at the same time one would expect to see the onset of the SPE less than 15 minutes after Earth. However, the event appeared to Mars as an Eastern event giving instruments in orbit and on the surface a poor connection to the field lines at the particle source. As a result, particles arrived 3.5

hours later than at the Earth possibly assisted by the presence of a Stream Interaction Region (SIR) reported by *Guo et al.* [2018]. The fluxes relative to those seen at Earth are therefore consistent with the location of the event on the solar disc and the relative location of the planets. *Guo et al.* [2018] also report that the drop in particle intensity at lower energies towards the end of the SPE seen at the Earth also likely resulted from an SIR which acted as a boundary between the source (now well past 1 AU) and the in-situ detectors. Unlike the in-situ measurements made from the Earth, the magnetic connection to the observing detectors at Mars is continuing to improve throughout this time and with it the particle access. As a result, the lower energy (15 - 100 MeV) particles measured by MAVEN (seen in the top panel of Figure 22) continue to increase until the shock passes Mars which likely occurred some time on 13th September. This is consistent with a reduction seen in high energy particle fluxes measured by the MSL-RAD instrument on the Martian surface (seen in the bottom panel of Figure 22) which is the result of a Forbush decrease as the CME passes the planet attenuating the flux of the Galactic Cosmic Ray (GCR) background. The Forbush decrease is also detectable in the 80 - 200 MeV MAVEN measurement at the same time. The difference in the timing of the commencement and peak of the flux enhancement between the MAVEN and MSL data stems from the impact of the Martian atmosphere which has a thickness of $\sim 23 \mathrm{g.cm.}^{-2}$ which requires a proton energy of at least 150 MeV to reach the RAD detector on MSL on the surface. As the CME-driven shock strength reduces, the shock is no longer capable of accelerating particles to energies which can be detected on the surface of Mars. So even though the connection is improving the flux decreases well before the shock arrival. The 80 - 220 MeV detector on MAVEN is an intermediate case being enhanced due to

improved magnetic connection but ultimately reducing before the passage of the shock due to its weakening. The secondary neutrons detected by the HEND instrument on Mars Odyssey (Figure 21 (c)) reflect a similar trend to the this higher energy MAVEN detector.

We also present the measured dose quantities at ISS altitudes. The total ISS dose was equal to 67.8 μGy compared to 369 μGy measured on the surface of Mars by RAD. This reflects the additional geomagnetic shielding afforded by the Earth as well as the comparable physical shielding provided by the ISS with respect to the Martian atmosphere. Despite detectable rapid increases in dose rates this event would be too small to represent a risk to the health of an astronaut receiving it although much larger SPEs are possible and could cause problematic dose levels [*Zeitlin et al.*, 2018]. By use of the ground-based neutron monitor data a dose has been calculated for aircraft altitudes showing a dose level increase for polar orbits although once more this event did not pose a health risk to airline crew and passengers.

Spacecraft component ionising dose levels calculated and presented herein demonstrate that the contribution of such an event would not have large implications for design processes and are certainly within the expectations of SEP specification models for modest confidence levels (e.g. *Jiggens et al.* [2018]). However, anomalies resulting from Single Event Effects (SEEs), which have been shown to be well correlated with the SPE, were observed on a range of satellites in Earth orbit.

Acknowledgments.

NOAA's NCEI (National Centers for Environmental Information) is the authoritative provider for original GOES data which can be accessed here:

https://www.ngdc.noaa.gov/stp/satellite/goes/

The work to derive the effective energies for the GOES/EPEAD instrument was supported under ESA Contract No. 4000108377/13/NL/AK. Along with extensive cleaning of the data to correct for caveats, this resulting in the SEPEM Reference Data Set (RDS). Version 2.1 of the RDS can be found here:

http://sepem.eu/help/SEPEM_RDS_v2-01.zip

The work to derive cross-calibrated fluxes for the Proba-1/SREM and INTEGRAL/IREM data was support under ESA Contract No. 21480/08/NL/NR.

The authors are grateful to the PROBA-V/EPT teams at B.USOC and ESA/Redu for deep involvement in the data acquisition process. The CSR team also thanks P. Coquay, J. Nijskens, H. Verbeelen, and W. Verschueren at the Belgian Science Policy - Space Research and Applications (BELSPO) for support to the PRODEX project entitled "PROBA-V/EPT- Data Exploitation-Extension", ESA/PRODEX PEA N∘ C4000107617.

National Institute of Information and Communications Technology (Japan) is acknowledged for providing access to Space Environment Data Acquisition Monitor (SEDA) data. SEDA data analysis was supported by ESA Contract No. 4000119253/17/NL/LF/hh.

The RPS work was supported by NASA Van Allen Probes science funding through JHU/APL on contract NNN0601C. RPS sensor data are available from the Virtual Radiation Belt Observatory at virbo.org/RBSP/RPS.

The work to derive the GLE fluxes and aircraft doses was supported by the Academy of Finland (project No. 272157, Center of Excellence ReSoLVE and project No. 267186) and the UK Science and Technology Facilities Council (grant No. ST/N000749/1).

At DLR, Cologne, DOSIS 3D was supported by the DLR grant FuE-Projekt "ISS LIFE" (Programm RF-FuW, Teilprogramm 475).

This work was supported at the NASA Johnson Space Center by the NASA Human Health and Performance Contract, #NNJ15HK11B. The MSL-RAD project is supported in the United States by the National Aeronautics and Space Administration's Human Exploration and Operations Mission Directorate, under Jet Propulsion Laboratory subcontract #1273039 to Southwest Research Institute, and in Germany by the German Aerospace Center (DLR) and DLR's Space Administration grant numbers 50QM0501, 50QM1201, and 50QM1701 to the Christian Albrechts University, Kiel.

The work to derive Electro-L2 and Meteor-M2 data was supported by the Russian Science Foundation (Grant No. 16-17-00098).

The authors thank J.J Plaut for providing the Mars Odyssey HEND data.

References

Band, D., J. Matteson, L. Ford, B. Schaefer, D. Palmer, B. Teegarden, T. Cline, M. Briggs, W. Paciesas, G. Pendleton, G. Fishman, C. Kouveliotou, C. Meegan, R. Wilson, and P. Lestrade (1993), BATSE observations of gamma-ray burst spectra. I - spectral diversity, *The Astrophysical Journal*, *413*(1), 281–292.

Barabash, S., and R. Lundin (2006), ASPERA-3 on Mars Express, *Icarus*, *182*(2), 301–307.

Berger, T., S. Burmeister, D. Matthiä, B. Przybyla, G. Reitz, B. P., and et al. (2017), DOSIS & DOSIS 3D: radiation measurements with the DOSTEL instruments on-board the Columbus Laboratory of the ISS in the years 2009-2016, *Journal of Space Weather and Space Climate*, *7*(A8), doi:https://doi.org/10.1051/swsc/2017005.

Berger, T., D. Matthiä, S. Burmeister, R. Rios, E. Lee, K. Semones, and et al. (2018), The Solar Particle Event on 10 September 2017 as observed on-board the International Space Station (ISS), *Space Weather*, *16*, doi:https://doi.org/10.1029/2018SW001920.

Boynton, W. V., and et al. (2004), The mars odyssey gamma-ray spectrometer instrument suite, *Space Science Review*, *110*, 3783.

Crosby, N., D. Heynderickx, P. Jiggens, A. Aran, B. Sanahuja, P. Truscott, F. Lei, C. Jacobs, S. Poedts, S. Gabriel, I. Sandberg, A. Glover, and A. Hilgers (2015), SEPEM: A tool for statistical modeling the solar energetic particle environment, *Space Weather*, *13*, 406–426.

Cyamukungu, M., S. Benck, and S. Borisov (2014), The Energetic Particle Telescope (EPT) on Board PROBA-V: Description of a New Science-Class Instrument for Particle Detection in Space, *IEEE Transactions on Nuclear Science*, *61*, 3667–3681.

Guo, J., M. Dumbovic, R. Wimmer-Schweingruber, M. Temmer, H. Lohf, Y. Wang, A. Veronig, D. Hassler, L. Mays, C. Zeitlin, B. Ehresmann, O. Witasse, J. Freiherr von Forstner, B. Heber, M. Holmstrm, and A. Posner (2018), Modeling the evolution and propagation of the 2017 September 9th and 10th CMEs and SEPs arriving at Mars constrained by remote-sensing and in-situ measurement, *Space Weather*, pp. arXiv:1803.00,461v3 [physics.space–ph].

Hassler, D. M., C. Zeitlin, R. F. Wimmer-Schweingruber, S. Bottcher, C. Martin, J. Andrews, and et al. (2012), The radiation assessment detector (RAD) investigation, *Space Science Reviews*, *170*, 503–558, doi:https://doi.org/10.1007/s11214-012-9913-1.

Hassler, D. M., C. Zeitlin, B. Ehresmann, R. F. Wimmer-Schweingruber, J. Guo, D. Matthiä, S. Rafkin, T. Berger, and G. Reitz (2018), Space Weather on the Sur-

face of Mars: Impact of the September 2017 Events, *Space Weather*.

Jiggens, P., A. Varotsou, P. Truscott, D. Heynderickx, F. Lei, H. Evans, and E. Daly (2018), The solar accumulated and peak proton and heavy ion radiation environment (SAPPHIRE) model, *IEEE Transactions on Nuclear Science*, *65*(2), 698–711.

Kataoka, R., T. Sato, S. Miyake, D. Shiota, and Y. Kubo (2018), Radiation dose nowcast for the ground level enhancement on 10-11 September 2017, *Space Weather*, *16*.

Kestilä, A., T. Tikka, P. Peitso, J. Rantanen, A. Näsilä, K. Nordling, H. Saari, R. Vainio, P. Janhunen, J. Praks, and M. Hallikainen (2013), Aalto-1 nanosatellite - technical description and mission objectives, *Geoscientific Instrumentation, Methods and Data Systems*, *2*, 121–130, doi:10.5194/gi-2-121-2013.

Kurt, V., A. Belov, K. Kudela, and B. Yushkov (2018), Some characteristics of gle on 10 september 2017, *Contributions of the Astronomical Observatory Skalnat Pleso*, *48*, 329–338, doi:https://arxiv.org/pdf/1806.00226.pdf.

Lee, C. O., B. M. Jakosky, J. G. Luhmann, D. A. Brain, M. L. Mays, D. M. Hassler, M. Holmström, D. E. Larson, D. L. Mitchell, C. Mazelle, and J. S. Halekas (2018), Observations and impacts of the 10 September 2017 solar events at Mars: An overview and synthesis of the initial results, *Geophysical Research Letters*, *45*, 887–8885, doi: https://doi.org/10.1029/2018GL079162.

Malandraki, O. E., and N. B. Crosby (2018), *Solar Particle Radiation Storms Forecasting and Analysis: The HESPERIA HORIZON 2020 Project and Beyond*, Springer.

Matthiä, D., M. M. Meier, and T. Berger (2018), The solar particle event on 10-13 september 2017 - spectral reconstruction and calculation of the radiation exposure in aviation and space, *Space Weather*, *16*, doi:https://doi.org/10.1029/2018SW001921.

Mewaldt, R. A., C. M. S. Cohen, A. W. Labrador, R. A. Leske, G. M. Mason, M. I. Desai, M. D. Looper, J. E. Mazur, R. S. Selesnick, and D. K. Haggerty (2005), Proton, helium, and electron spectra during the large solar particle events of October-November 2003, *Journal of Geophysical Research*, *110*(A09S18).

Mishev, A., and I. Usoskin (2015), Numerical model for computation of effective and ambient dose equivalent at flight altitudes: Application for dose assessment during GLEs, *Journal of Space Weather and Space Climate*, *5*(3), doi:10.1051/swsc/2015011.

Mishev, A., and I. Usoskin (This issue), Assessment of radiation environment at commercial jet flight altitudes during GLE 72 on September 10, 2017, *Space Weather*.

Müller, D., B. Nicula, S. Felix, F. Verstringe, B. Bourgoignie, A. Csillaghy, D. Berghmans, P. Jiggens, J. P. García-Ortiz, J. Ireland, S. Zahniy, and B. Fleck (2017), JHelioviewer: Time-dependent 3D visualisation of solar and heliospheric data, *Astronomy and Astrophysics*, *606*, A10.

Nagatsuma, T., K. Sakaguchi, Y. Kubo, P. Belgraver, F. Chastellain, R. Muff, and T. Otomo (2017), The space environment data acquisition monitor on board himawari-8 as space environment monitoring on japanese meridian of geo, *Earth, Planets and Space*, *69*(74), doi:doi:10.1186/s40623-017-0659-6.

O'Brien, T., J. Mazur, and M. Looper (This issue), Solar energetic proton access to the magnetosphere during the 10-14 september 2017 particle event, *Space Weather*.

Reames, D. V. (1999), Particle acceleration at the sun and in the heliosphere, *Space Science Reviews*, *90*, 413–491.

Redmon, R. J., D. B. Seaton, R. Steenburgh, J. He, and J. V. Rodriguez (2018), September 2017s geoeffective space weather and impacts to Caribbean radio communications

during hurricane response, *Space Weather*, *16*, https://doi.org/10.1029/2018SW001897.

Rodriguez, J. V., T. G. Onsager, and J. E. Mazur (2010), The East–West effect in solar proton flux measurements in geostationary orbit: A new goes capability, *Geophysical Research Letters*, *37*, L07,109.

Rodriguez, J. V., J. C. Krosschell, and J. C. Green (2014), Intercalibration of goes 815 solar proton detectors, *Space Weather*, *12*, 92–109.

Rodriguez, J. V., I. Sandberg, R. A. Mewaldt, I. A. Daglis, and P. Jiggens (2017), Validation of the effect of cross-calibrated goes solar proton effective energies on derived integral fluxes by comparison with stereo observations, *Space Weather*, *15*, 290–309.

Ryden, K. A., A. D. P. Hands, C. I. Underwood, and D. J. Rodgers (2015), Internal Charging Measurements in Medium Earth Orbit Using the SURF Sensor, *IEEE Transactions on Plasma Science*, *43*(9).

Sandberg, I., I. Daglis, A. Anastasiadis, P. Bühler, P. Nieminen, and H. Evans (2012), Unfolding and validation of SREM fluxes, *IEEE Transactions on Nuclear Science*, *59*, 1105–1112.

Sandberg, I., P. Jiggens, D. Heynderickx, and I. Daglis (2014), Cross calibration of NOAA GOES solar proton detectors using corrected NASA IMP-8/GME data, *Geophysical Research Letters*, *41*, 4435–4441.

Schwadron, N. A., F. Rahmanifard, J. Wilson, A. P. Jordan, H. E. Spence, C. J. Joyce, J. B. Blake, A. W. Case, W. de Wet, W. M. Farrellm, J. C. Kasper, M. D. Looper, N. Lugaz, L. Mays, J. E. Mazur, J. Niehof, N. Petro, C. W. Smith, W. Townsend, R. Winslow, and C. Zeitlin (2018), Update on the worsening particle radiation environment observed by CRaTER and implications for future human deep-space exploration.,

Space Weather, *16*, https://doi.org/10.1002/2017SW001803.

Seaton, D. B., and J. M. Darnel (2018), Observations of an eruptive solar flare in the extended EUV solar corona, *The Astrophysical Journal Letters*, *852*(1).

Smart, D. F., and M. A. Shea (1985), Handbook of geophysics (chapter 6: Galactic cosmic radiation and solar energetic particles).

Sun, X., and A. A. Norton (2017), Super-flaring Active Region 12673 Has One of the Fastest Magnetic Flux Emergence Ever Observed, *Research Notes of the American Astronomical Society*, *1*(1), 24, doi:10.3847/2515-5172/aa9be9.

Tylka, A. J., and W. F. Dietrich (2009), A new and comprehensive analysis of proton spectra in ground-level enhanced (GLE) solar particle events, *31st International Cosmic Ray Conference, Łódź*(Poland).

Van Allen, J. A., D. N. Baker, B. A. Randall, and D. D. Sentman (1974), The magnetosphere of jupiter as observed with pioneer 10: 1. instrument and principal findings, *Journal of geophysical research*, *79*(25).

Witasse, O., and et al. (2018), Investigating space weather events at mars with mars express housekeeping data, *52th Eslab symposium, ESTEC*.

Witasse, O., B. Sánchez-Cano, M. L. Mays, P. Kajdi, H. Opgenoorth, H. A. Elliott, I. G. Richardson, I. Zouganelis, J. Zender, R. F. Wimmer-Schweingruber, L. Turc, M. G. G. T. Taylor, E. Roussos, A. Rouillard, I. Richter, J. D. Richardson, R. Ramstad, G. Provan, A. Posner, J. J. Plaut, D. Odstrcil, H. Nilsson, P. Niemenen, S. E. Milan, K. Mandt, H. Lohf, M. Lester, J.-P. Lebreton, E. Kuulkers, N. Krupp, C. Koenders, M. K. James, D. Intzekara, M. Holmstrom, D. M. Hassler, B. E. S. Hall, J. Guo, R. Goldstein, C. Goetz, K. H. Glassmeier, V. Gnot, H. Evans, J. Espley, N. J. T. Edberg,

M. Dougherty, S. W. H. Cowley, J. Burch, E. Behar, S. Barabash, D. J. Andrews, and N. Altobelli (2017), Interplanetary coronal mass ejection observed at STEREO-A, Mars, comet 67P/Churyumov-Gerasimenko, Saturn, and New Horizons en route to Pluto: Comparison of its Forbush decreases at 1.4, 3.1, and 9.9 AU, *Journal of Geophysical Research*, *122*, 7865–7890.

Yan, X. L., J. C. Wang, G. M. Pan, D. F. Kong, Z. K. Xue, L. H. Yang, Q. L. Li, and X. S. Feng (2018), Successive X-class Flares and Coronal Mass Ejections Driven by Shearing Motion and Sunspot Rotation in Active Region NOAA 12673, *The Astrophysical Journal*, *856*, 79, doi:10.3847/1538-4357/aab153.

Zeitlin, C., D. M. Hassler, J. Guo, B. Ehresmann, R. F. Wimmer-Schweingruber, S. C. Rafkin, and et al. (2018), Investigation of the radiation hazard observed by rad on the surface of mars during the sept 2017 solar particle event, *Geophysical Research Letters*, *45*, 5845–5851, doi:https://doi.org/10.1029/2018GL077760.

Table 1. GOES-15/EPS/EPEAD and HEPAD differential proton energy channel definitions and derived effective energies for channels 2 - 7 (E_{eff}) in MeV.

EPEAD								HEPAD		
Ch.	E_l	E_u	E_{eff}	Ch.	E_l	E_u	E_{eff}	Ch.	E_l	E_u
1	0.8	4.0		5	40	80	46.62	8	350	420
2	4.0	9.0	6.643	6	80	165	103.7	9	420	510
3	9.0	15	12.61	7	165	500	154.6	10	510	700
4	15	40	20.55							

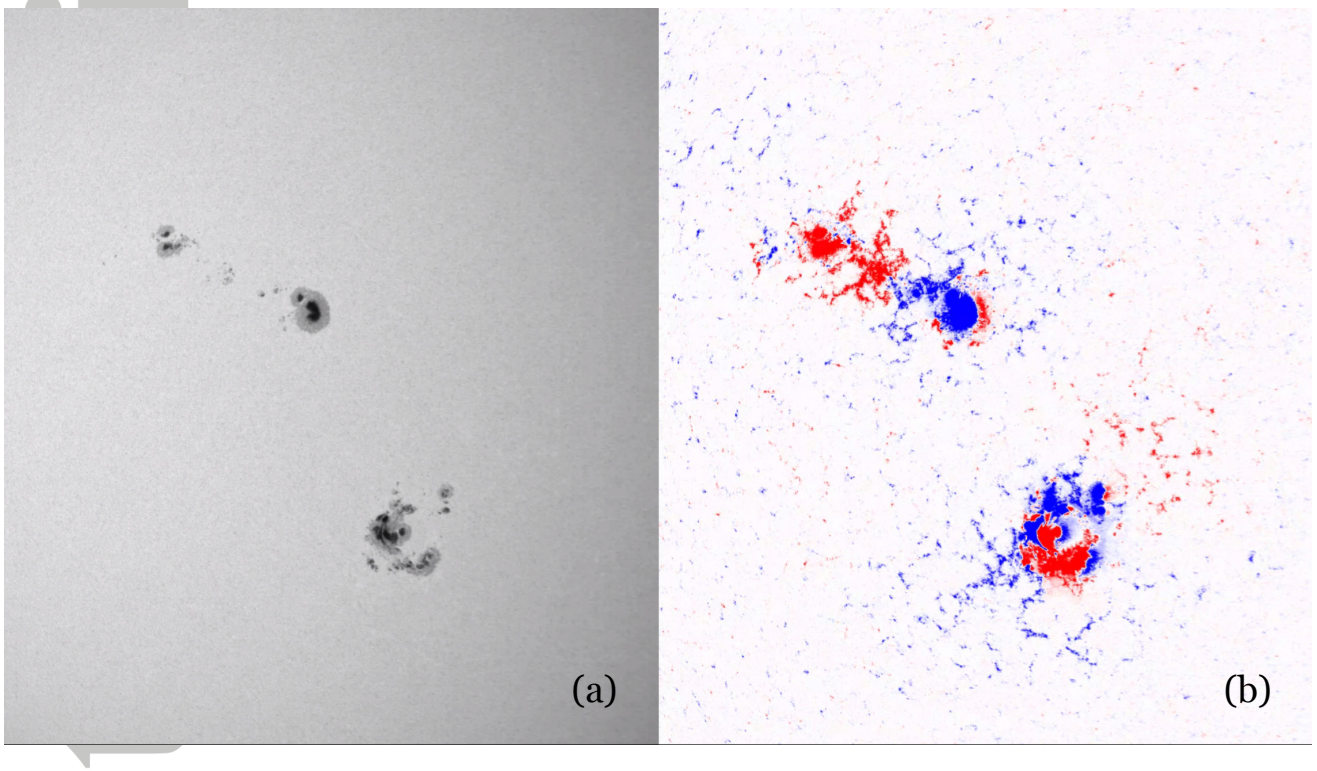

Figure 1. White light continuum image (left) and magnetogram image showing opposing polarities of the solar magnetic field in blue and red (right) recorded on 6th September 2017 as viewed by SDO/HMI showing AR 12674 (above) and AR 12673 (below).

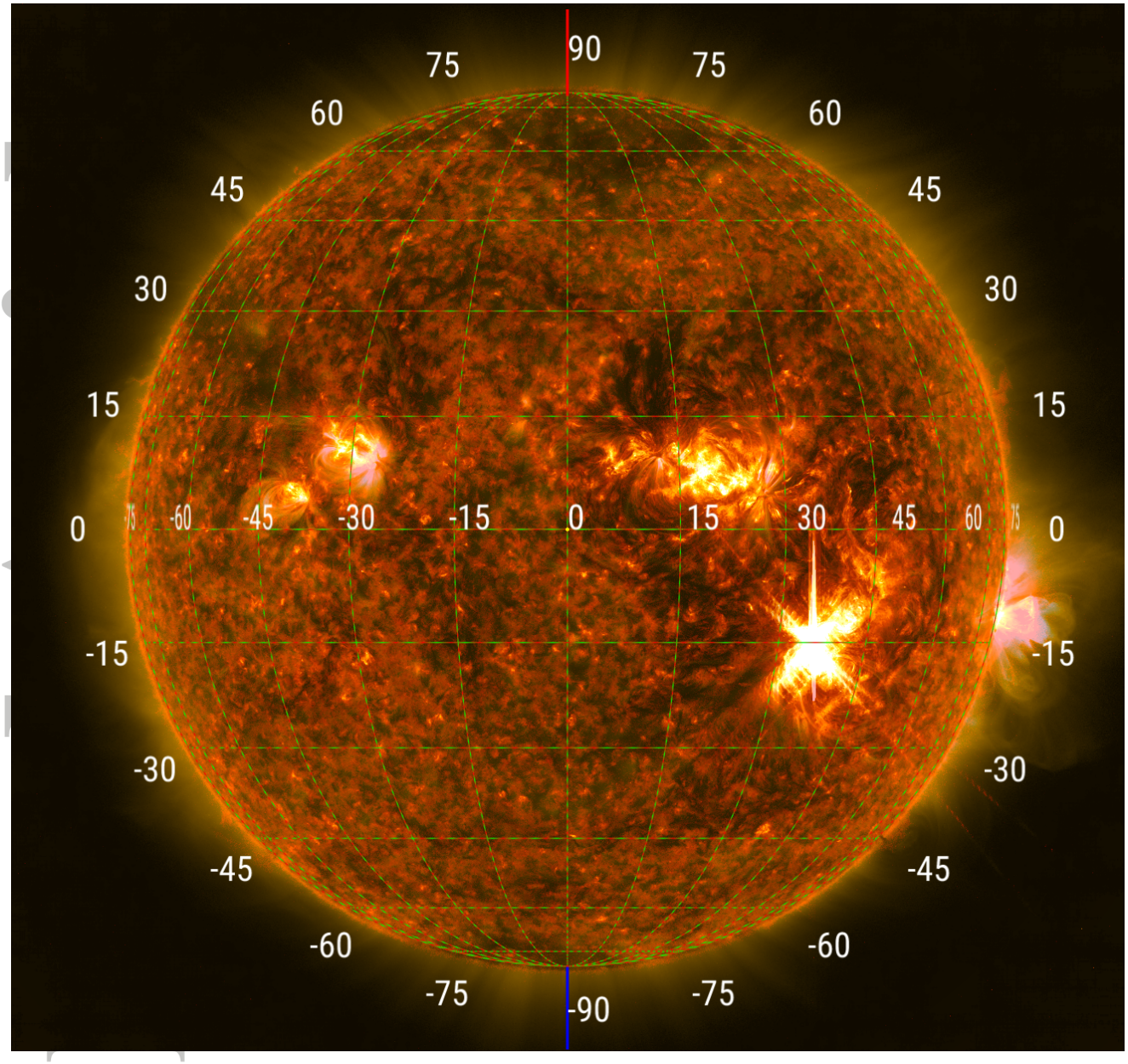

Figure 2. Composite image of onset of X9.3 flare recorded on 6th September 2017 as viewed by SDO/AIA in 171 Å and 304 Å wavelengths. The flare peak (as measured by the maximum X-ray flux in the 1 - 8 Å range) occurred at 12:02 UTC. (Solar North and South are indicated by the Red and Blue vertical line segments respectively)

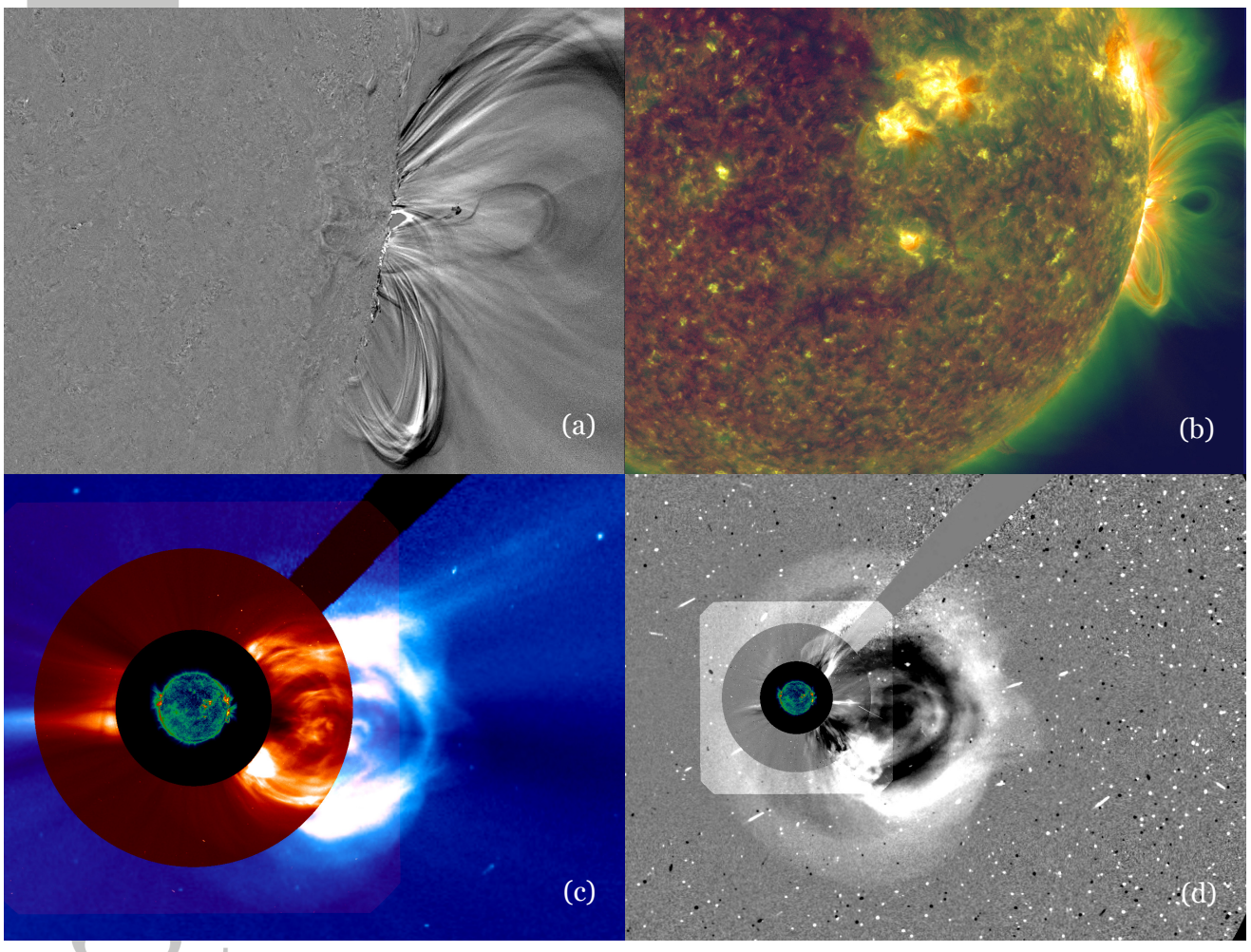

Figure 3. Images of the X8.2 flare and associated CME from 10th September 2017 with increasing field-of-view: Difference image of the flare and CME as viewed by SDO/AIA in 171 Å wavelength (top left); Composite image of the South-West region of the solar disc at the time of the flare as viewed by SDO/AIA in 171 Å, 211 Å and 304 Å wavelengths (top right); High contrast SDO/AIA 171 Å and SOHO/LASCO C2 and C3 coronagraph images extending to 11 solar radii centred around 16:15 UTC (bottom left); High contrast SDO/AIA 171 Å and SOHO/LASCO C2 and C3 difference images from 16:30 to 16:40 UTC images extending to 22 solar radii (bottom right) showing particle hits on the coronagraph images. (Solar North on all images is vertical upward direction)

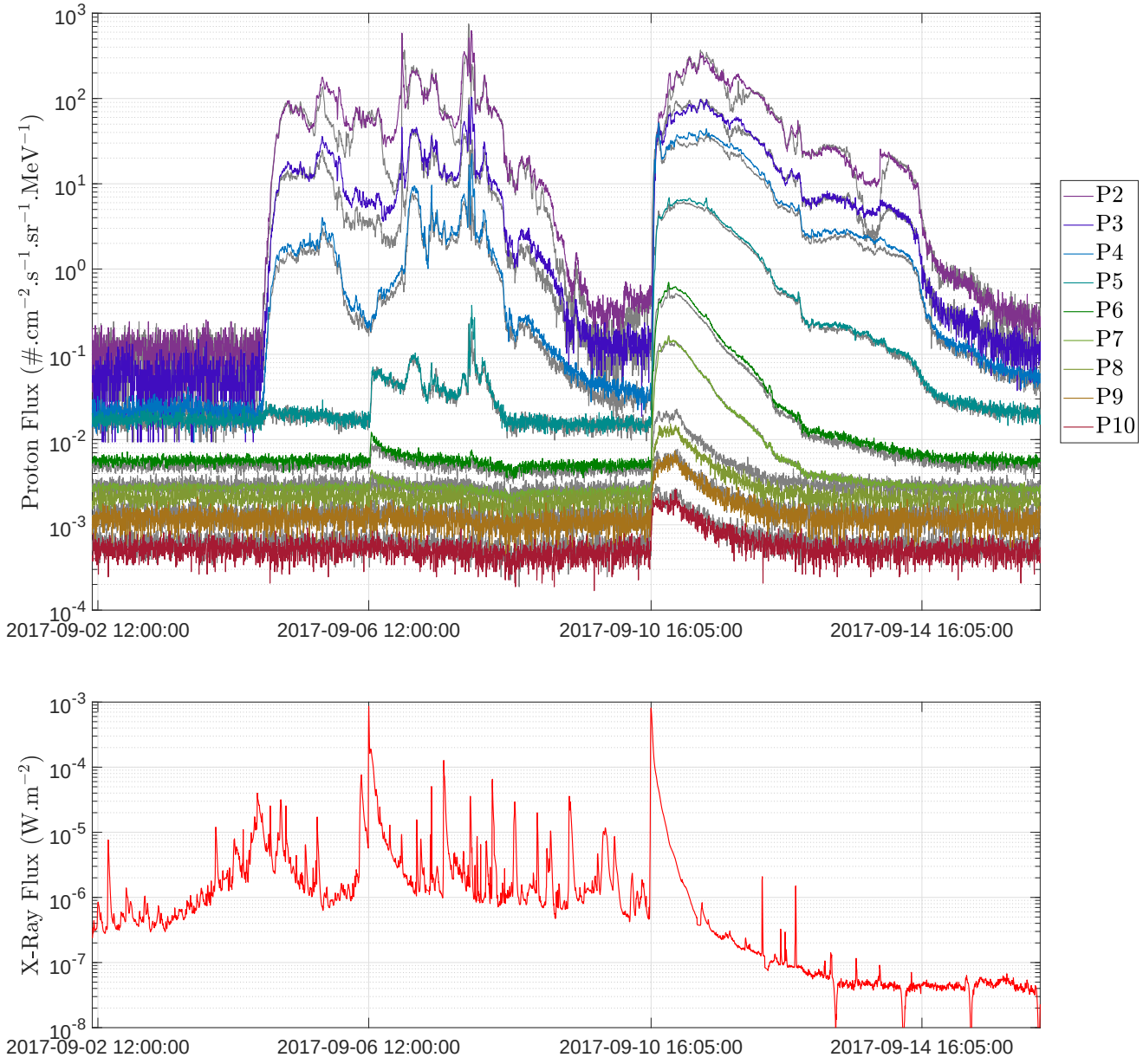

Figure 4. GOES-15/EPS differential fluxes from EPEAD West-facing and HEPAD detectors (colored lines) and East-facing detectors (grey lines) are shown in the top panel. GOES X-ray fluxes (1.0-8.0 Å) are shown in the bottom panel. Two vertical grid lines are selected to match the two X-class X-ray flare peaks to the nearest 5 minutes (the time resolution of the particle data), the two other vertical grid lines are 4 days before (after) these flare peaks.

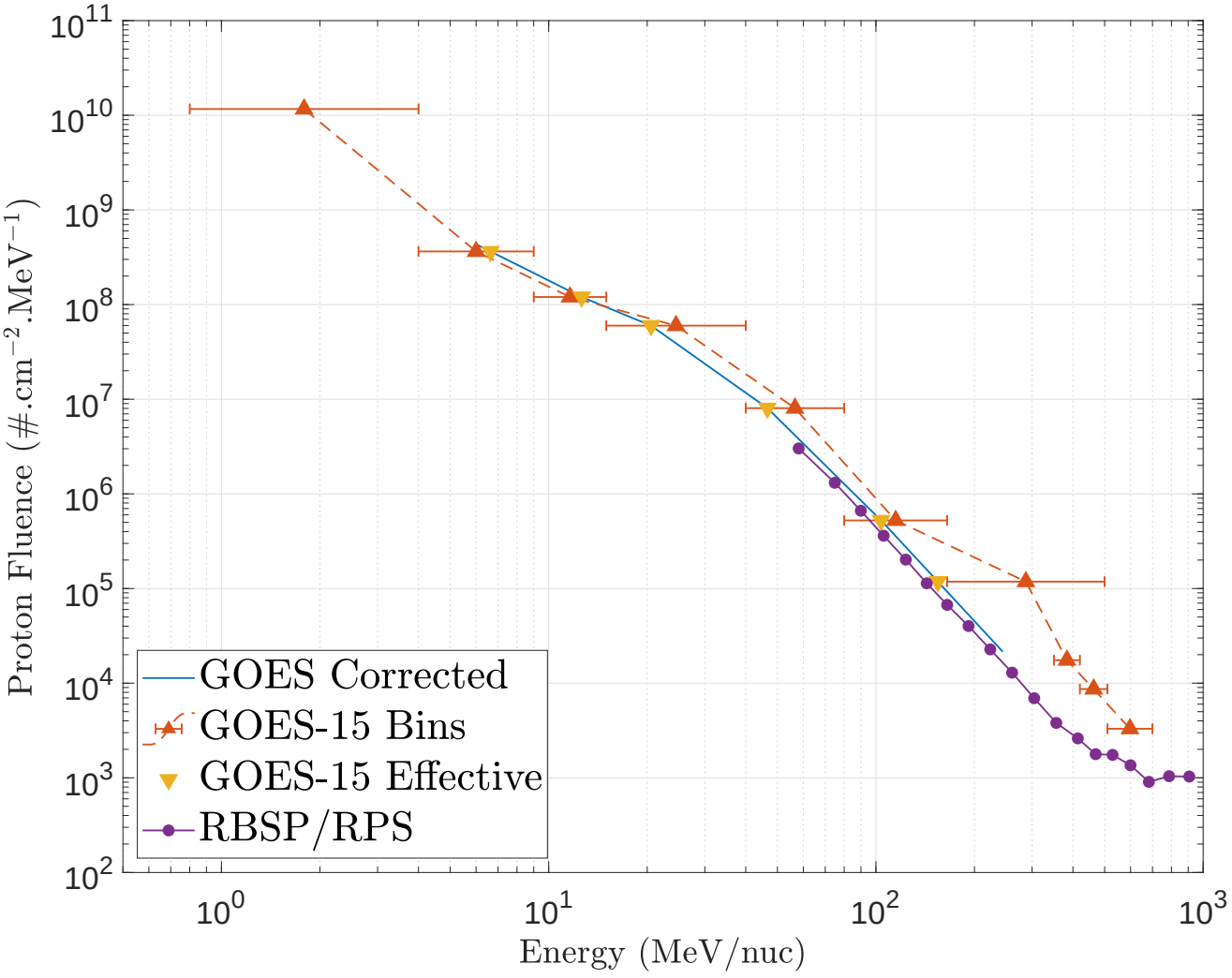

Figure 5. GOES-15/EPS differential fluxes with nominal energy bins are shown in red, the EPEAD bin effective energies as presented by [*Sandberg et al.*, 2014] are shown with yellow triangles and the resulting spectrum are shown with the blue line. Data from the RBSP/RPS instrument is shown in purple.

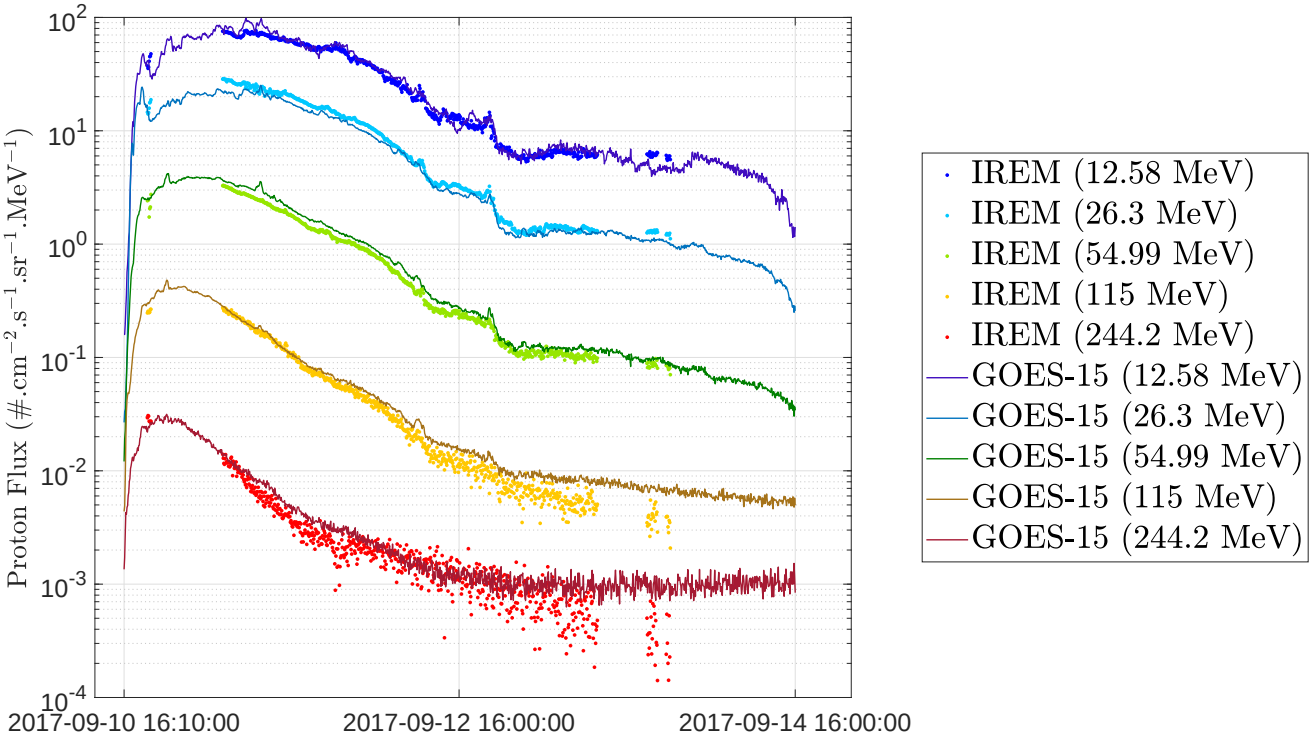

Figure 6. Corrected GOES-15/EPEAD differential fluxes compared to Level 2 data from INTEGRAL/IREM at 5 interpolated energies.

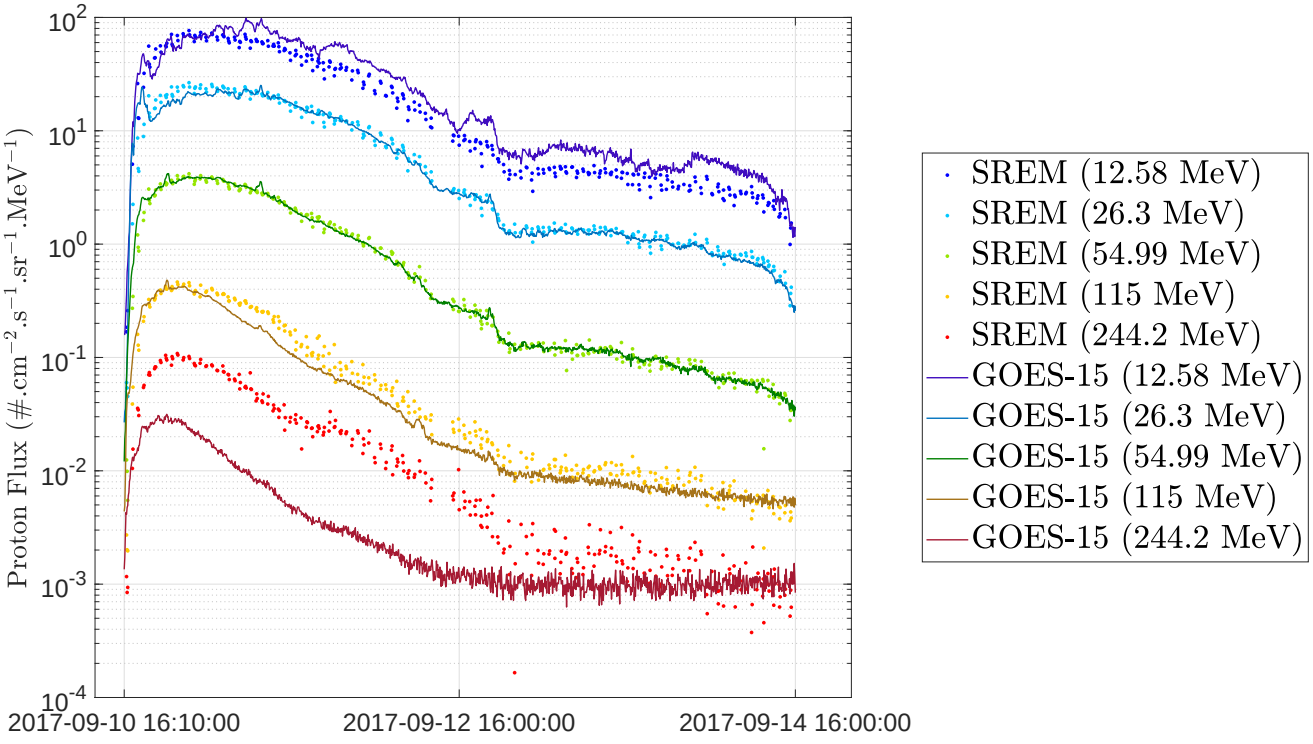

Figure 7. Corrected GOES-15/EPEAD differential fluxes compared to Level 2 data from Proba-1/SREM at 5 interpolated energies.

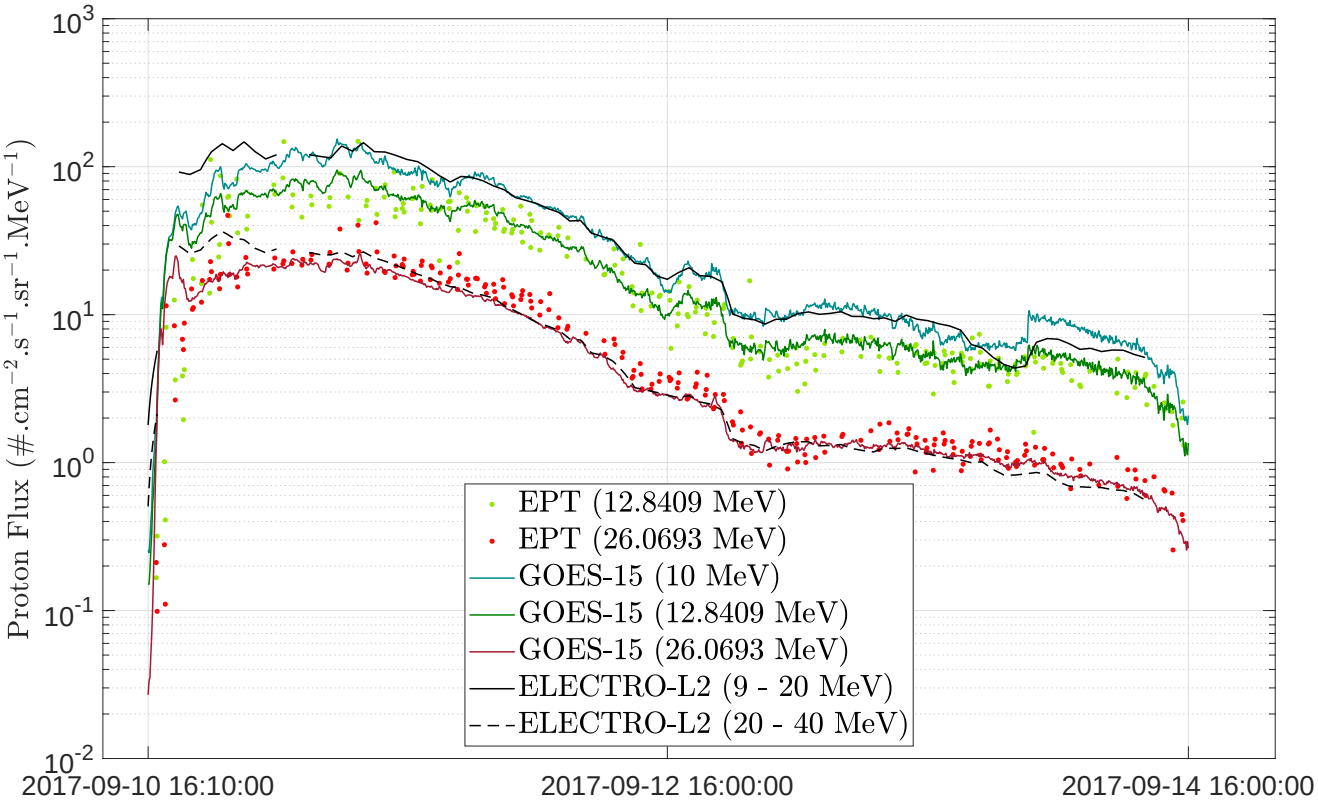

Figure 8. Corrected GOES-15/EPEAD differential fluxes compared to data from Proba-V/EPT and ELECTRO-L2 data interpolated to estimated ELECTRO-L2 mean energies.

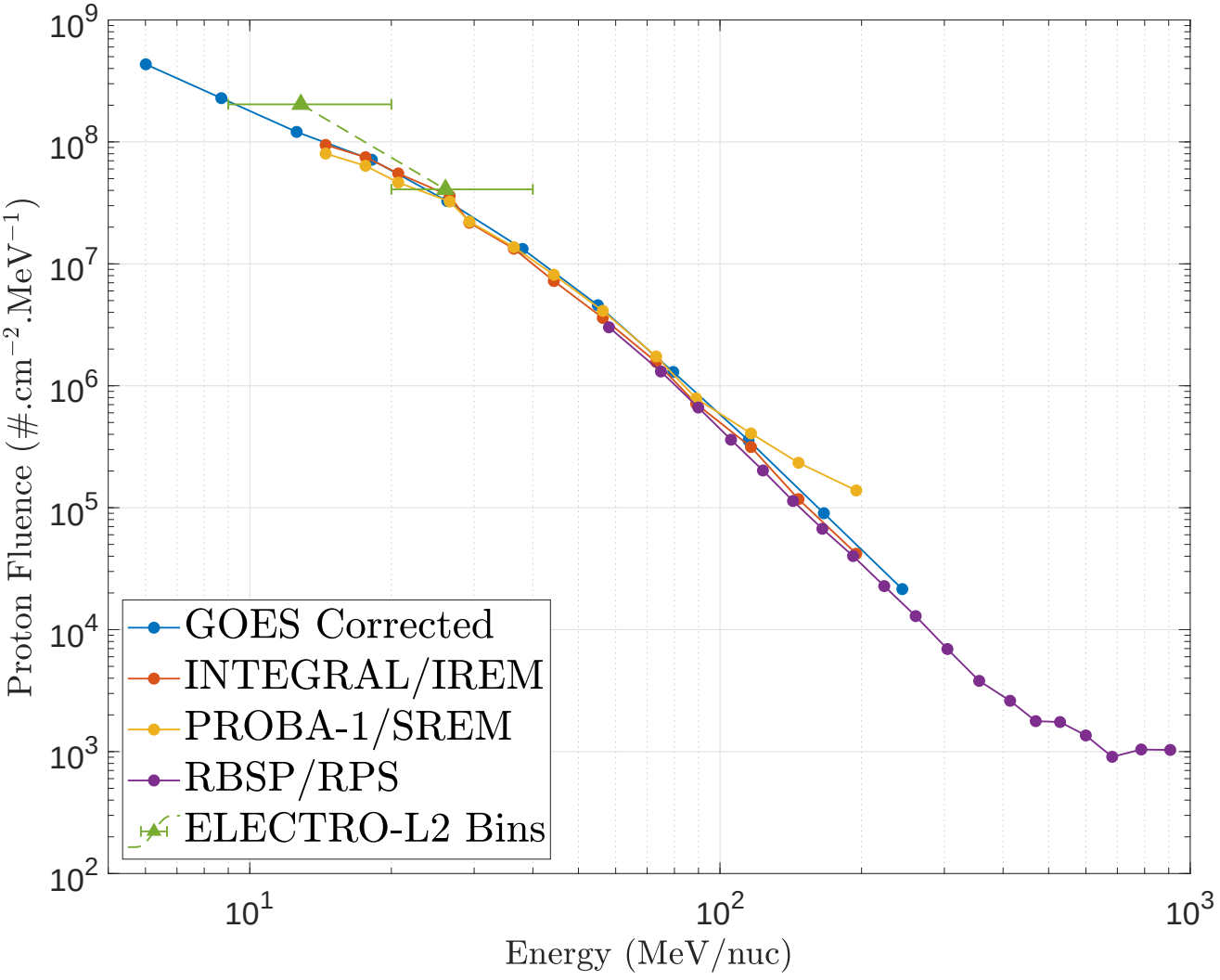

Figure 9. Differential fluence spectra of GOES-15/EPEAD compared to INTEGRAL/IREM, PROBA-1/SREM and ELECTRO data. Data from the RBSP/RPS instrument is shown in purple.

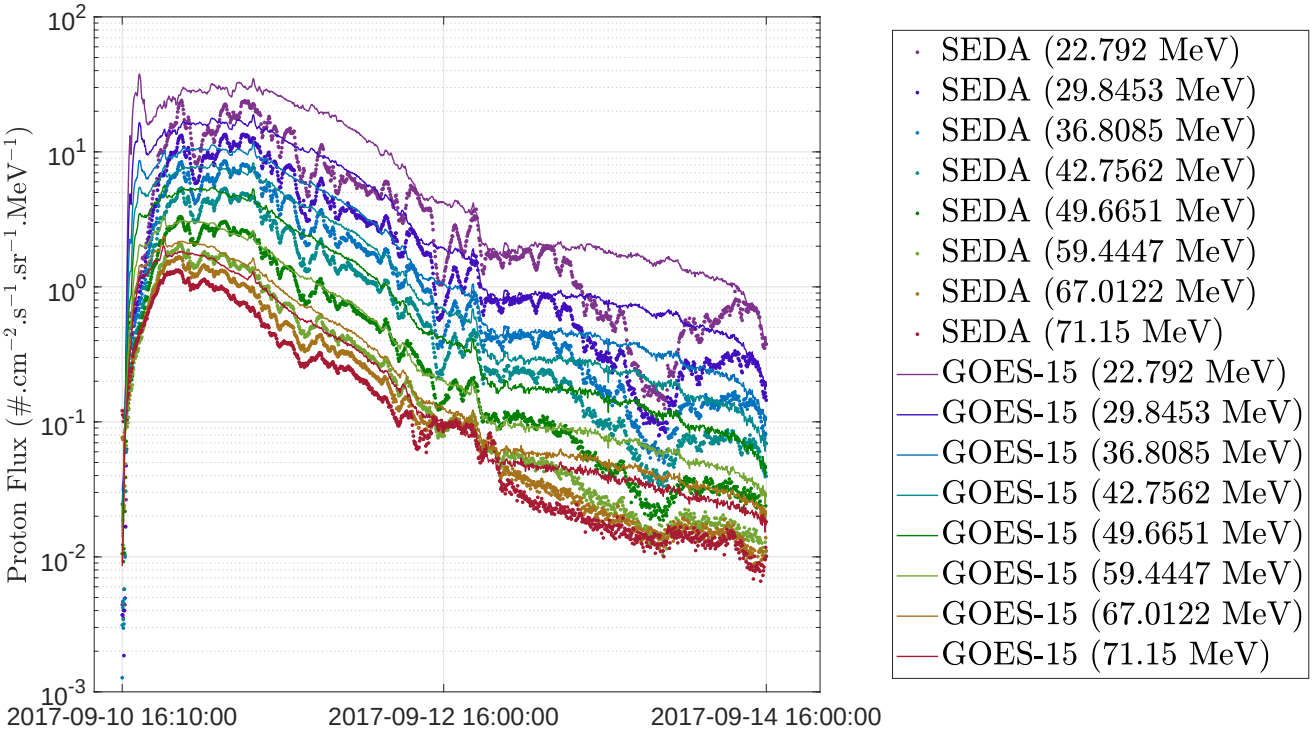

Figure 10. Data from Himawari-8/SEDA/PT (dots) compared to corrected GOES-15/EPEAD (lines) differential fluxes interpolated to SEDA channel mean energies. (N.B. the same colours are used for each energy for the different detectors)

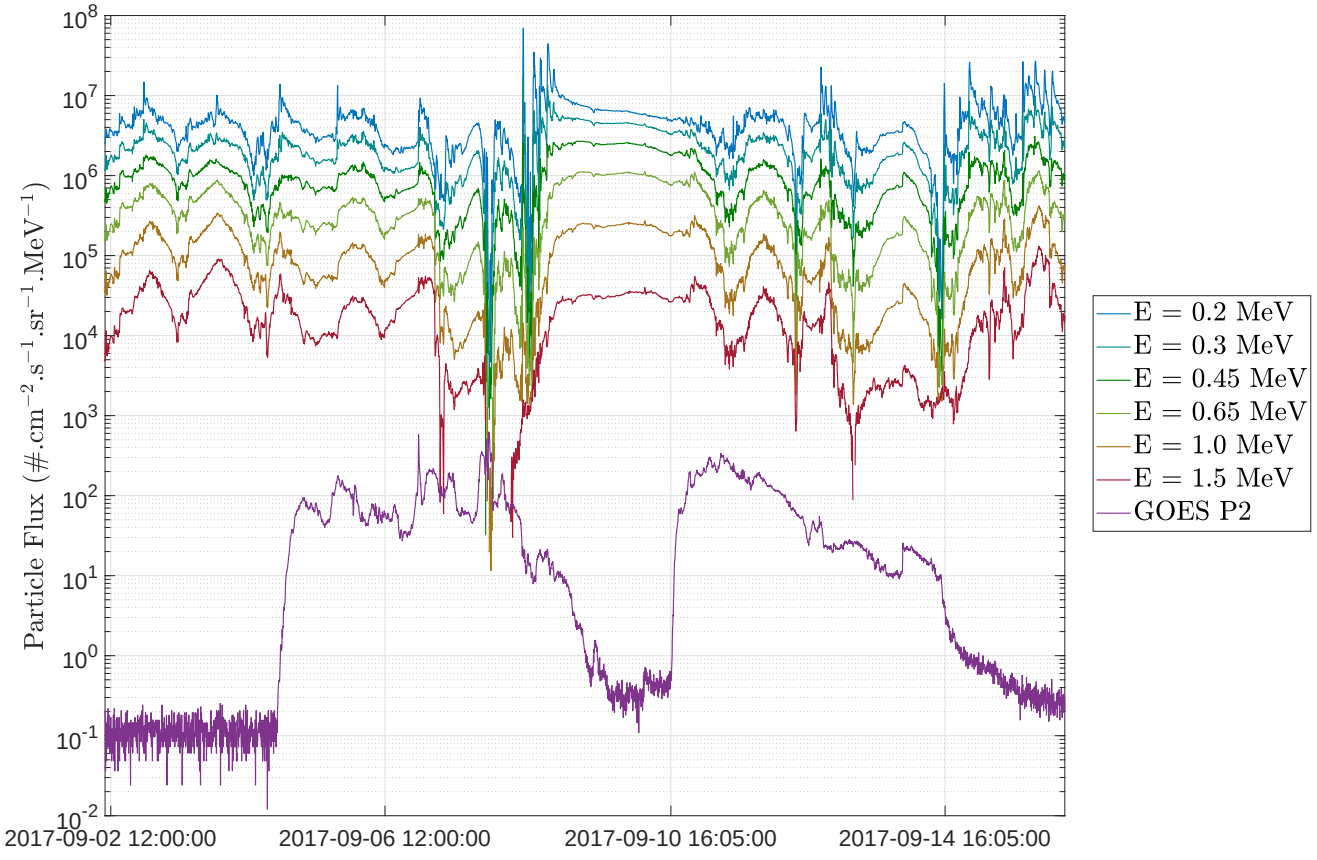

Figure 11. Data from Himawari-8/SEDA/SURF electron detector compared to corrected GOES-15/EPEAD differential fluxes in P2 (4-9 MeV).

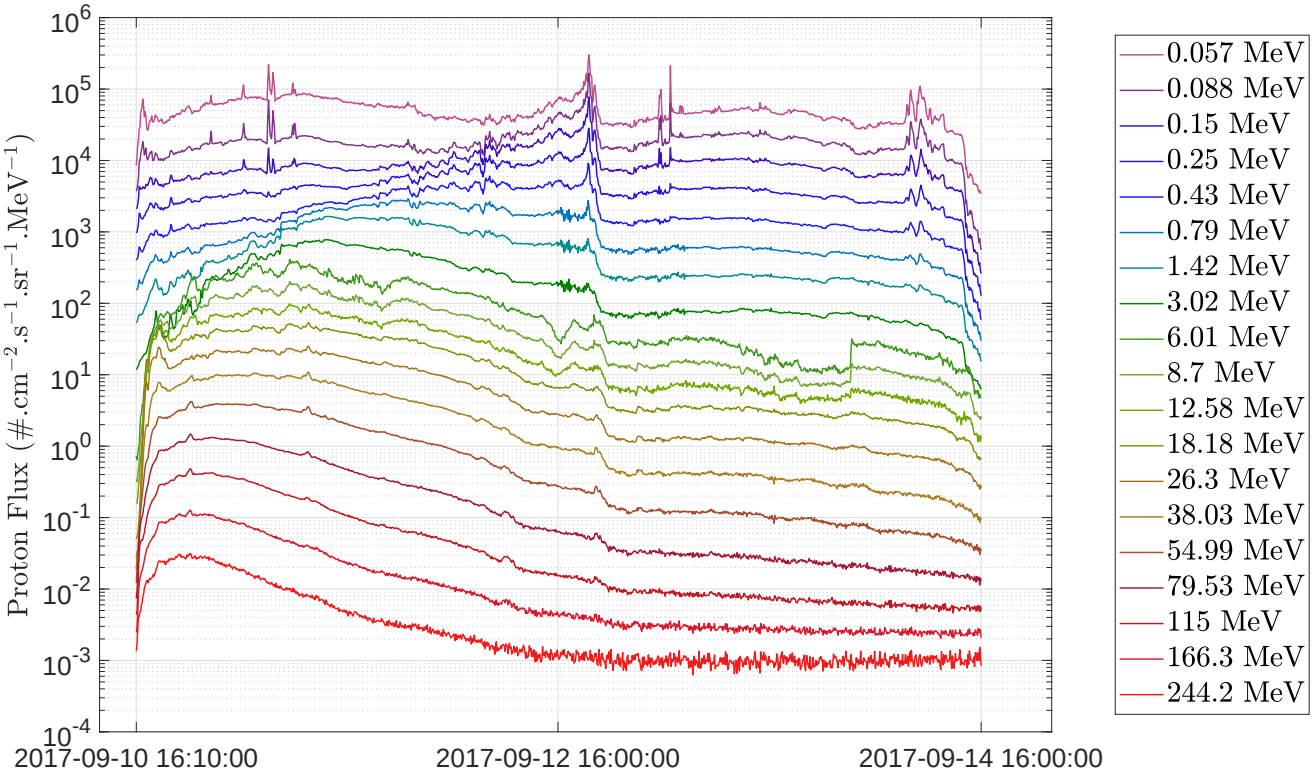

Figure 12. Differential fluxes from ACE/EPAM and GOES/EPEAD, The first 8 energies (up to 3.02 MeV) are taken from the EPAM instrument fluxes whilst the last 11 channels (6.01 MeV and above) are taken from the (corrected) EPEAD instrument fluxes.

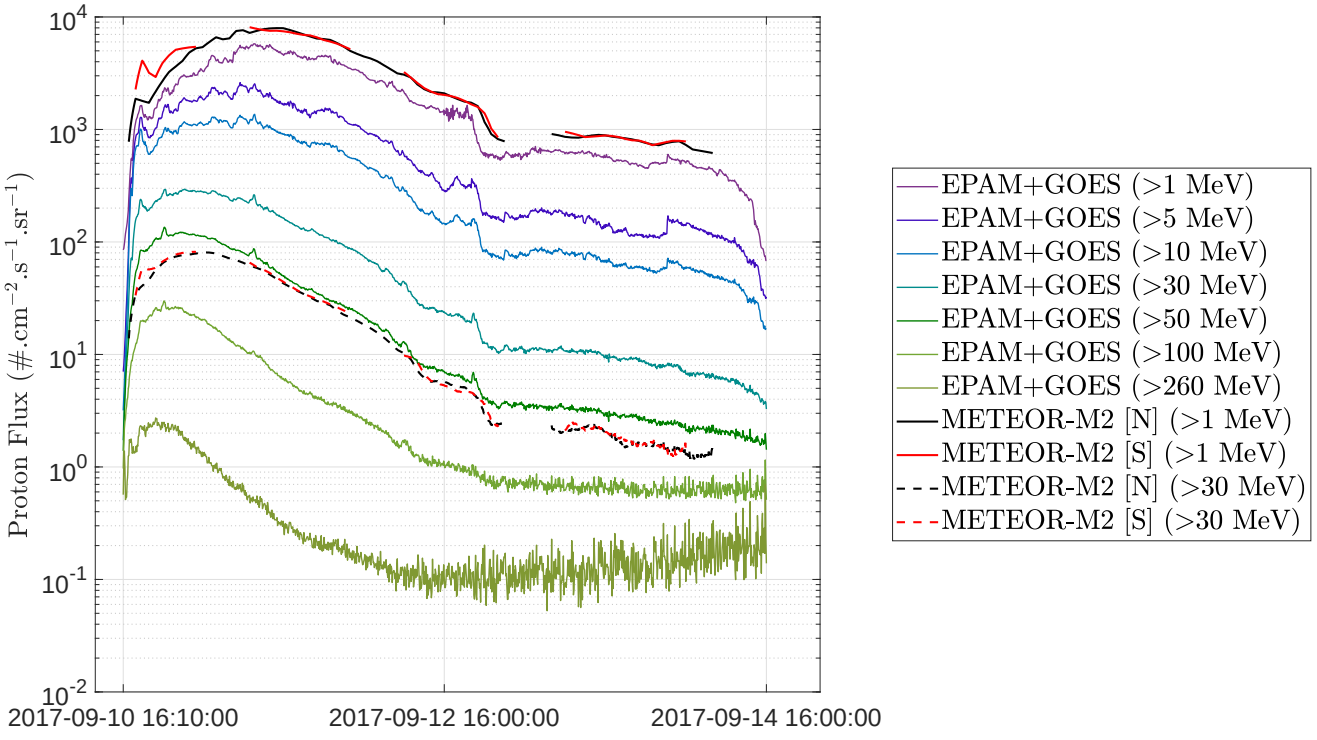

Figure 13. Integral fluxes derived from ACE/EPAM and GOES/EPEAD compared to data from two METEOR-M2 measurements in the Northern and Southren polar caps.

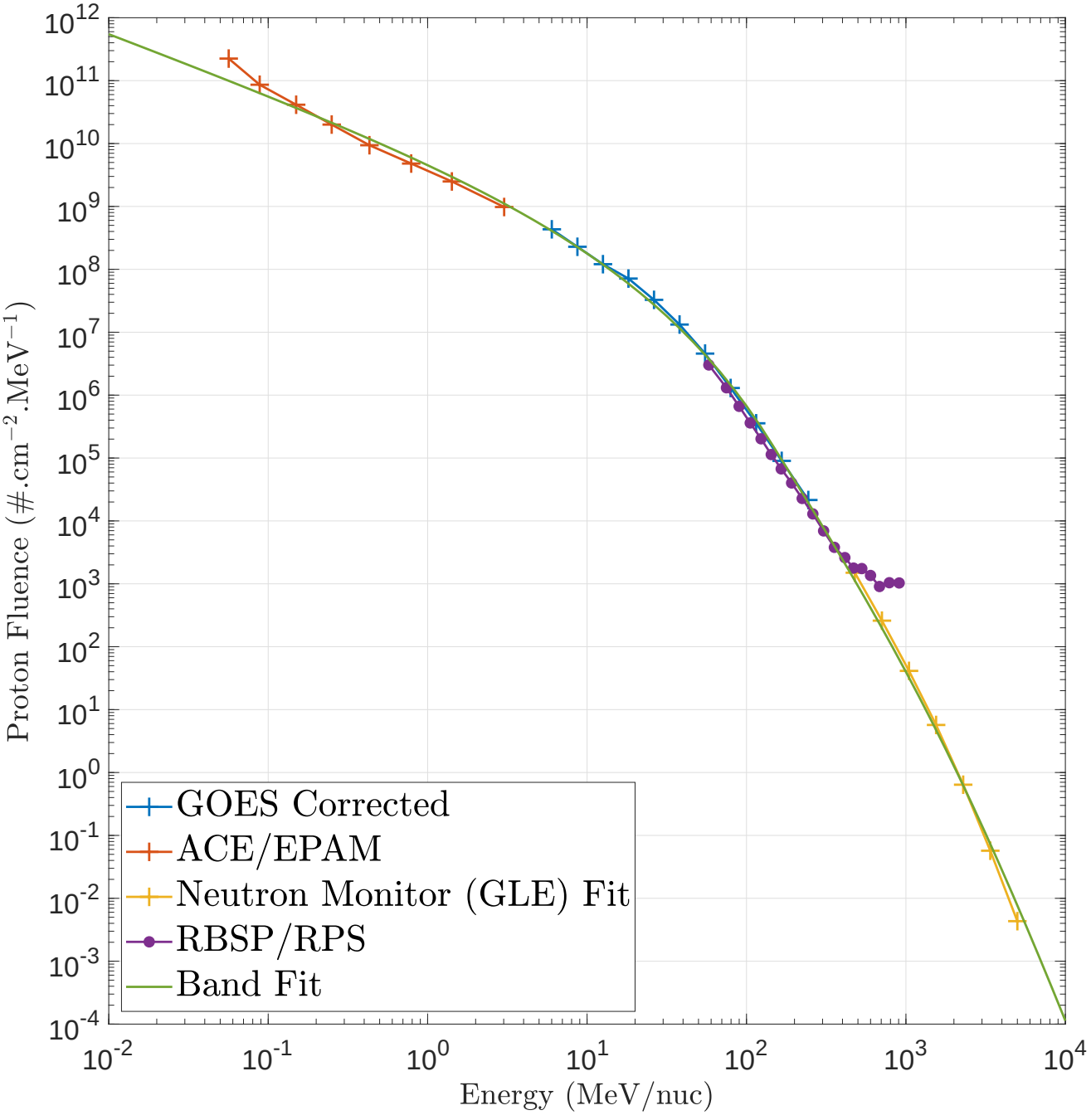

Figure 14. Full differential spectra for the SPE beginning on 10th September 2017 using data from ACE/EPAM, GOES-15/EPEAD and high-energy data determined from neutron monitor measurements. Data from the RBSP/RPS instrument are shown in purple and includes GCR fluxes.

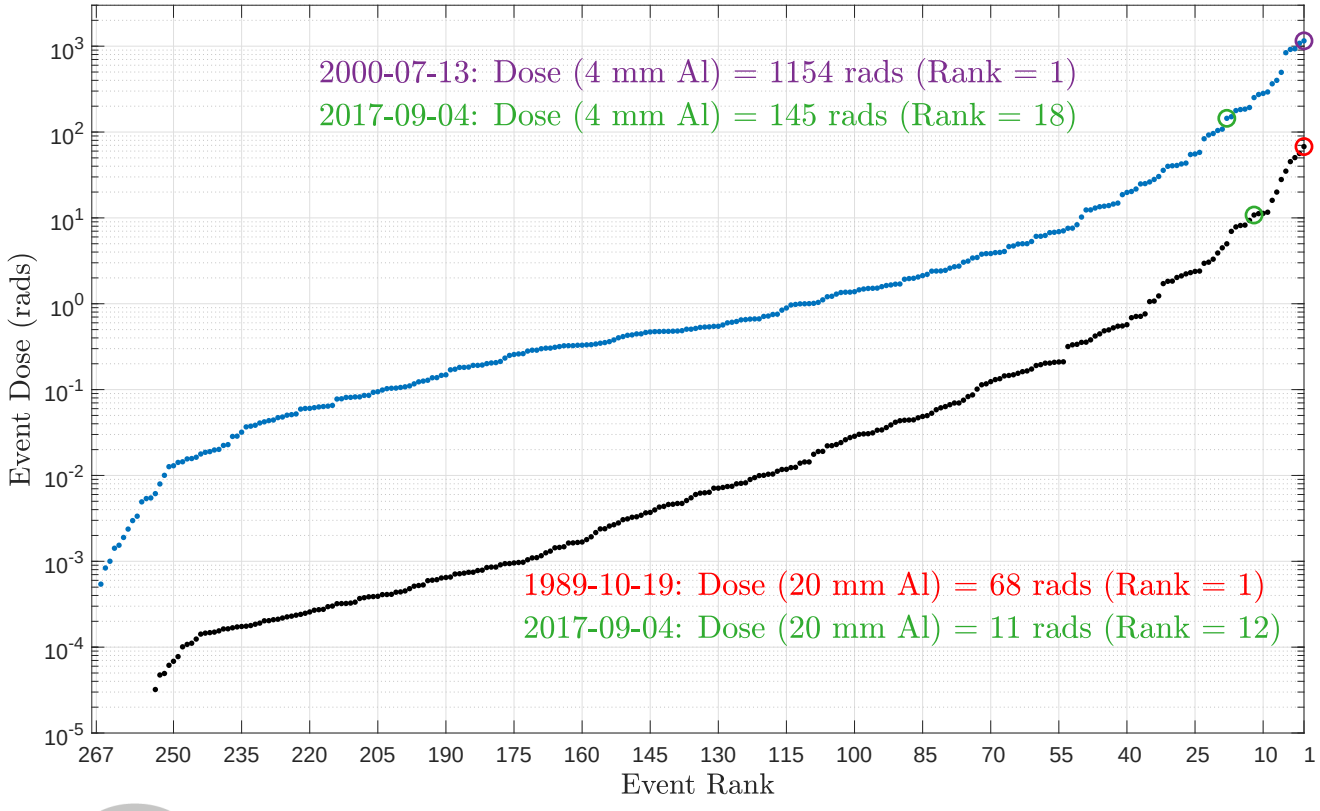

Figure 15. Cumulative distribution of ionising dose levels calculated using SHIELDOSE behind aluminium shielding of 4 mm (blue dots) and 20 mm (black dots) for all solar particle events from 1974 until mid-2015 with the addition of the SPE of early September 2017.

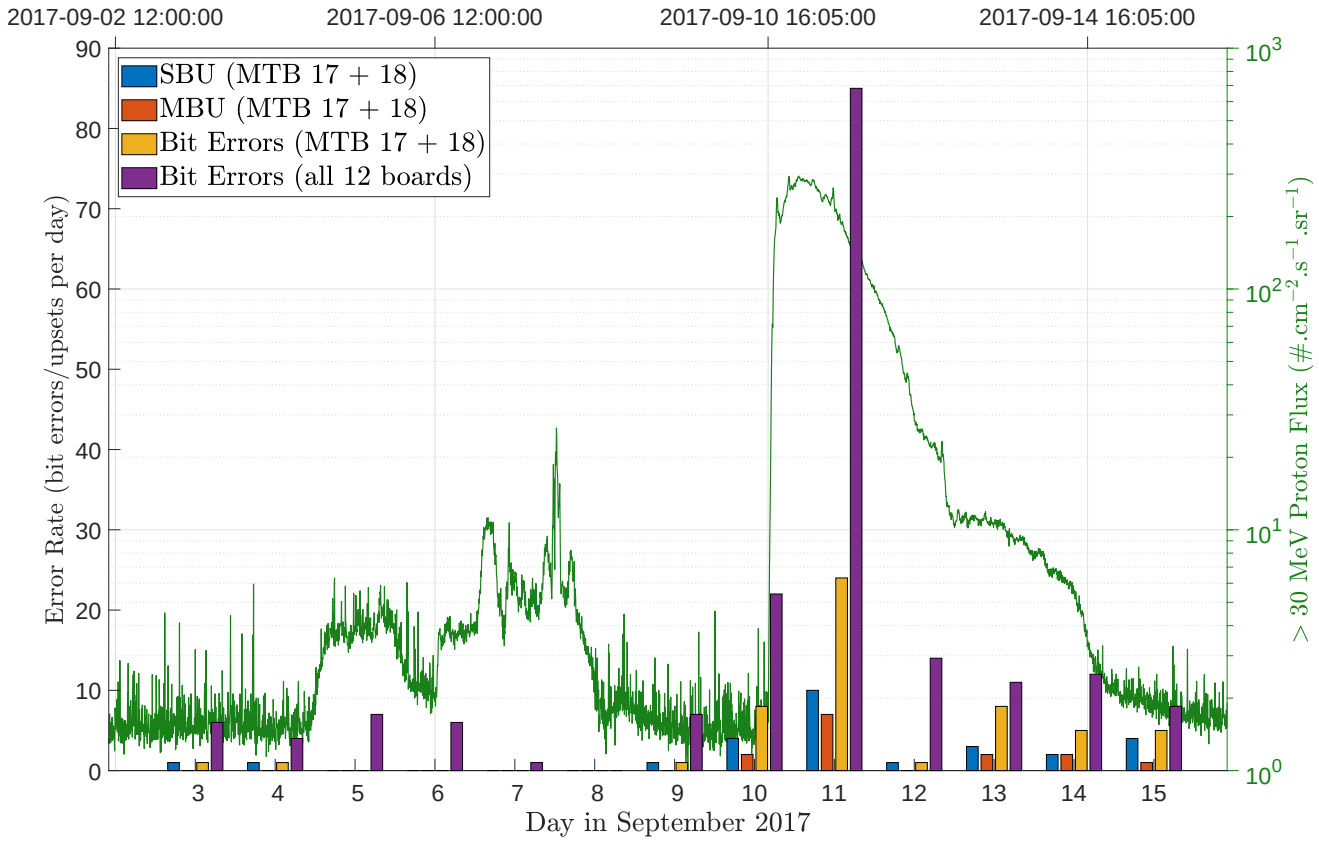

Figure 16. Single (SBU) and Multiple (MBU) Bit Upsets, and total bit errors in two memories on the Memory Test Board (MTB) flying on Alphasat plus the total bit errors on a total of 12 memories for each day from 3rd until 15th September 2017. Also plotted is the > 30 MeV proton flux has been calculated from GOES/EPEAD data as given in Figure 13.

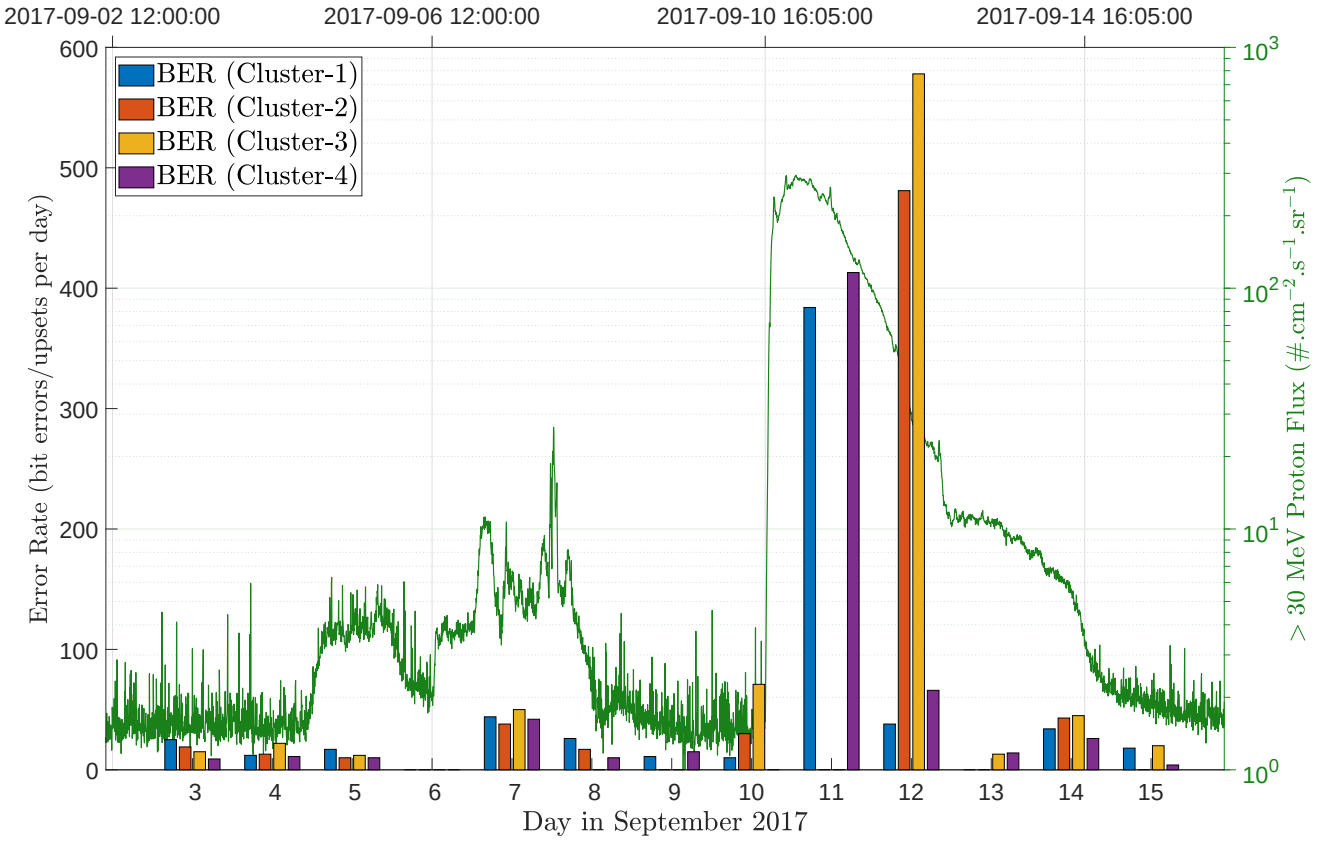

Figure 17. Bit Error Rate (BER) on a Solid State Recorder (SSR) on the Cluster spacecraft over a time period of 20 days. Also plotted is the > 30 MeV proton flux has been calculated from GOES/EPEAD data as given in Figure 13.

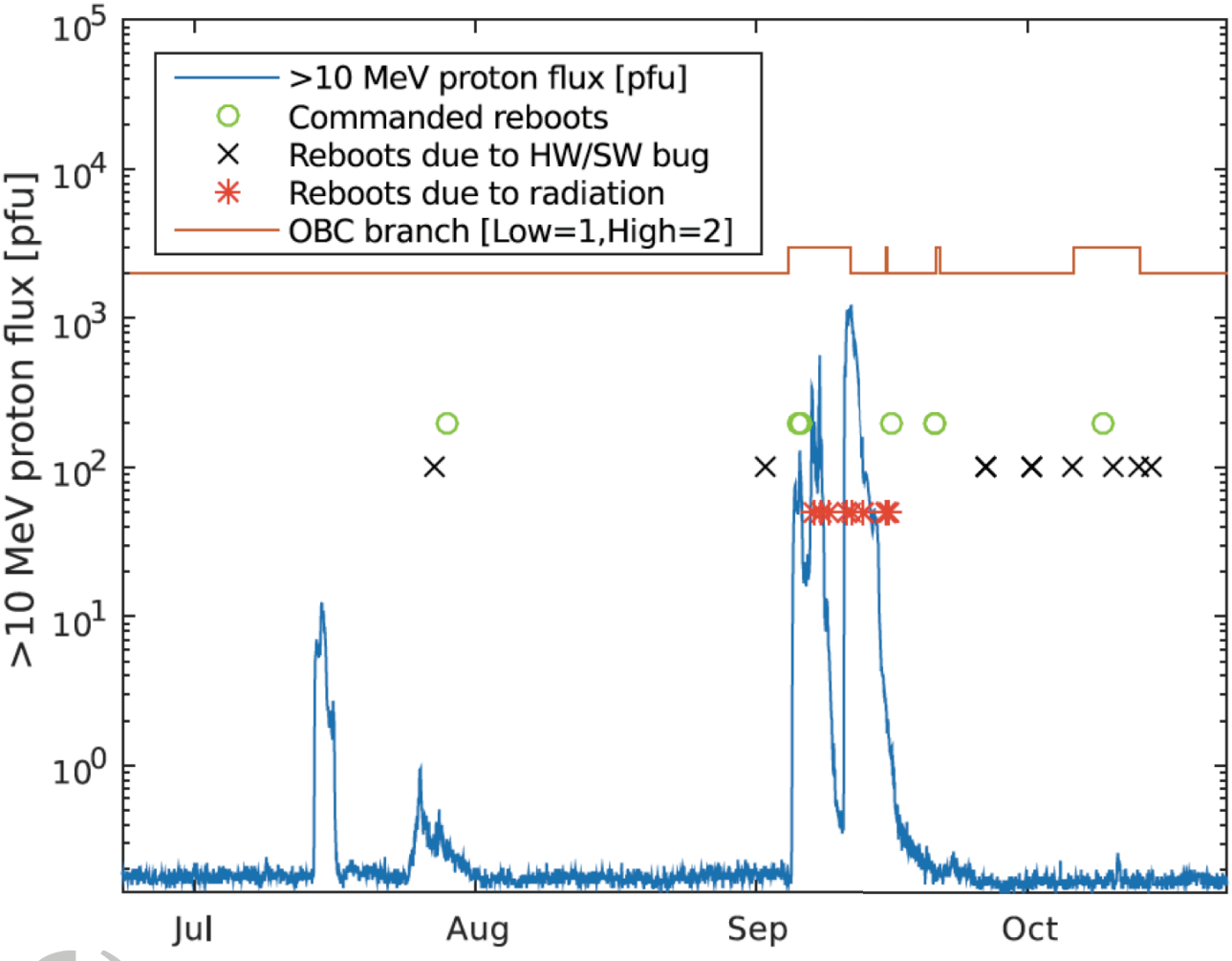

Figure 18. The GOES-15/EPEAD >10 MeV proton flux, the Aalto-1 OBC branch in use, and the reboots of the Aalto-1/OBC.

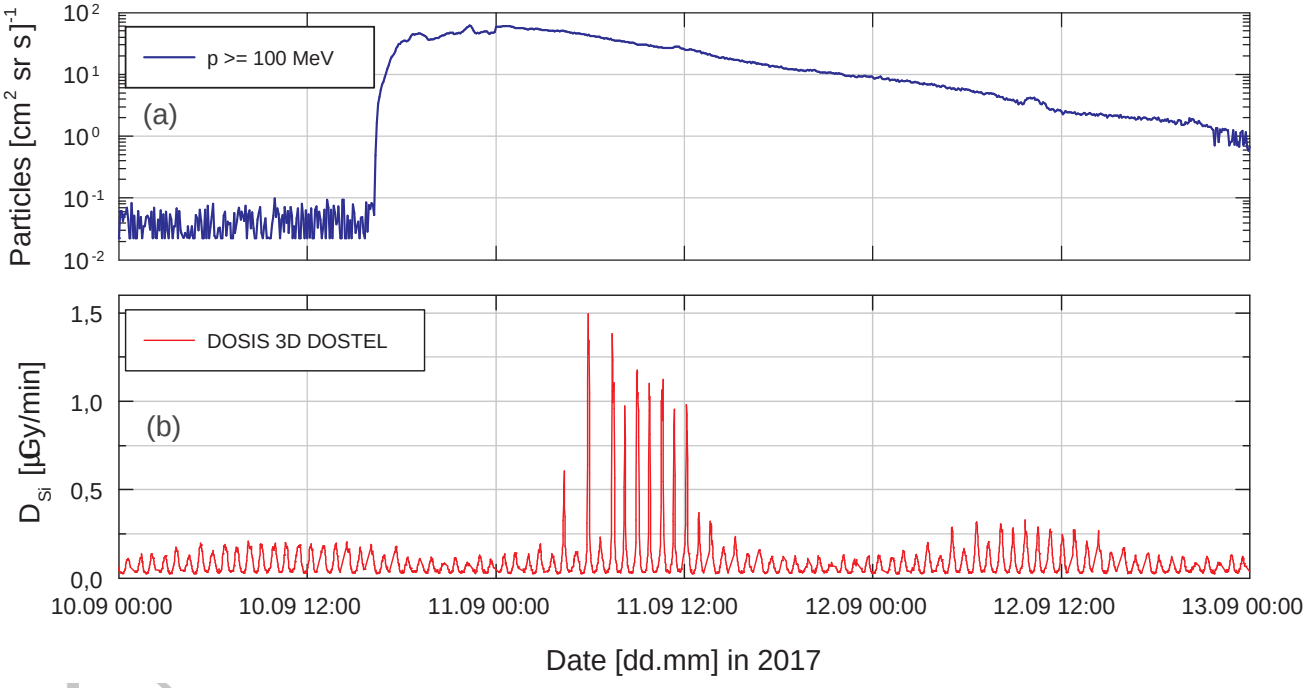

Figure 19. (a) GOES-15 proton flux > 100 MeV; (b) DOSIS 3D DOSTEL absorbed dose rate (in Si) for the 10th - 13th September 2017. Note: Relevant contributions from the South Atlantic Anomaly (SAA) crossings have been removed based on the procedure given in *Berger et al.* [2018]

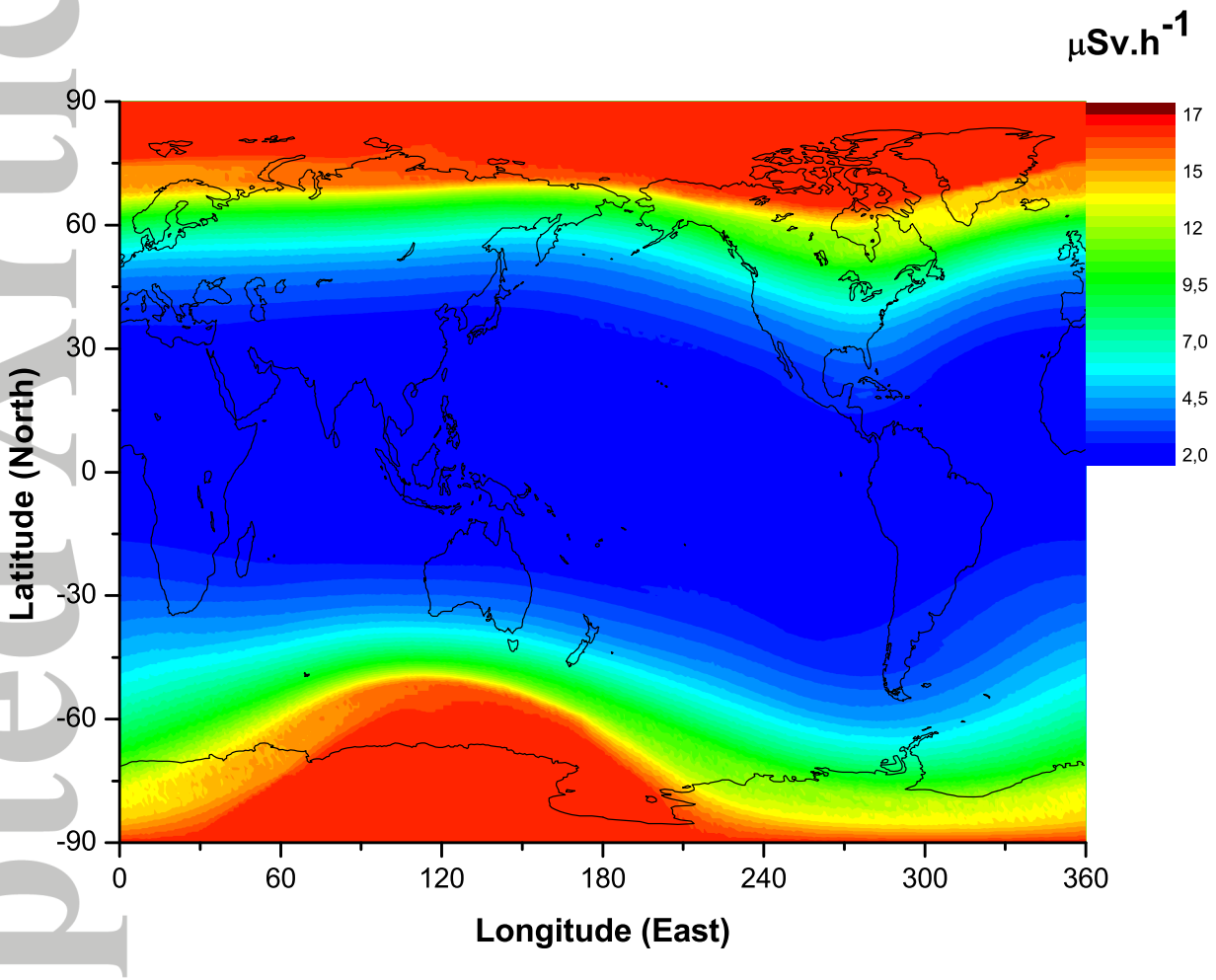

Figure 20. Doses at an aircraft altitude of 40000 feet (12.2 km) above sea level during the peak high-energy intensity of the September 2017 SPE (GLE 72).

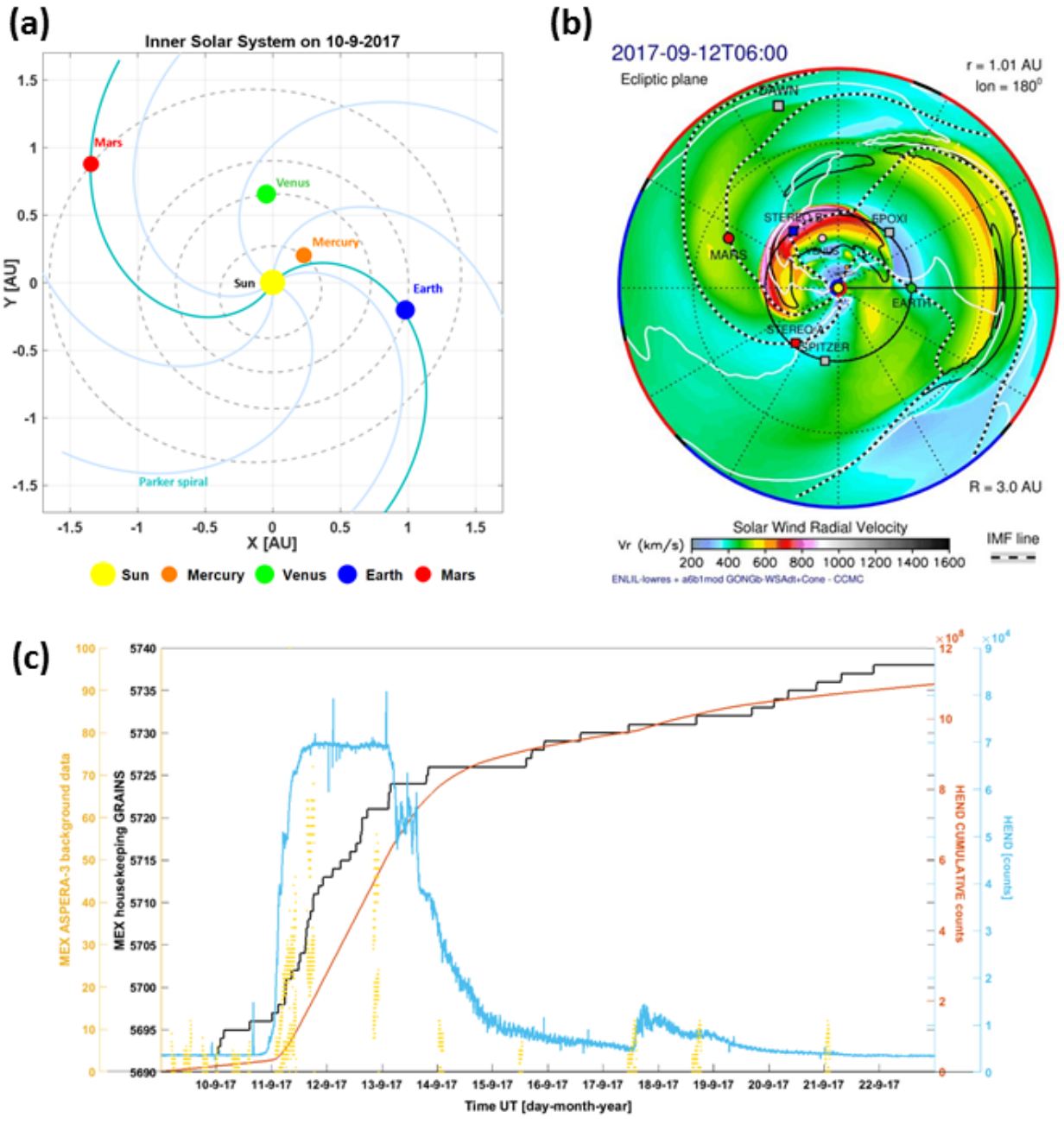

Figure 21. Panel (a) shows the planet positions in the inner solar system on 10th September 2017, with the Parker spiral simulated for a solar wind speed of 400 km/s. Panel (b) is a still image of the solar wind velocity in the ecliptic plane from a WSA-ENLIL + Cone model simulation (see [*Witasse et al.*, 2017] for references) showing the ICME that hit Mars on the 13th September. The full simulations are available at http://ccmc.gsfc.nasa.gov; run number: Leila Mays 120817 SH 9 [*Lee et al.*, 2018]. The colors represent the radial speed, as indicated in the color scale. Panel (c) displays some data acquired by satellites in orbit around Mars: in blue, the count rate of the HEND detector (scintillator block) on board Mars Odyssey [*Boynton and et al.*, 2004]; in red, its cumulative number; in yellow, the background of the IMA sensor from the ASPERA-3 instrument on-board Mars Express [*Barabash and Lundin*, 2006]; and in black, a housekeeping parameter from Mars Express (EDAC error counter) sensitive to space weather events [*Witasse and et al.*, 2018]. The space weather event is clearly identified with these data.

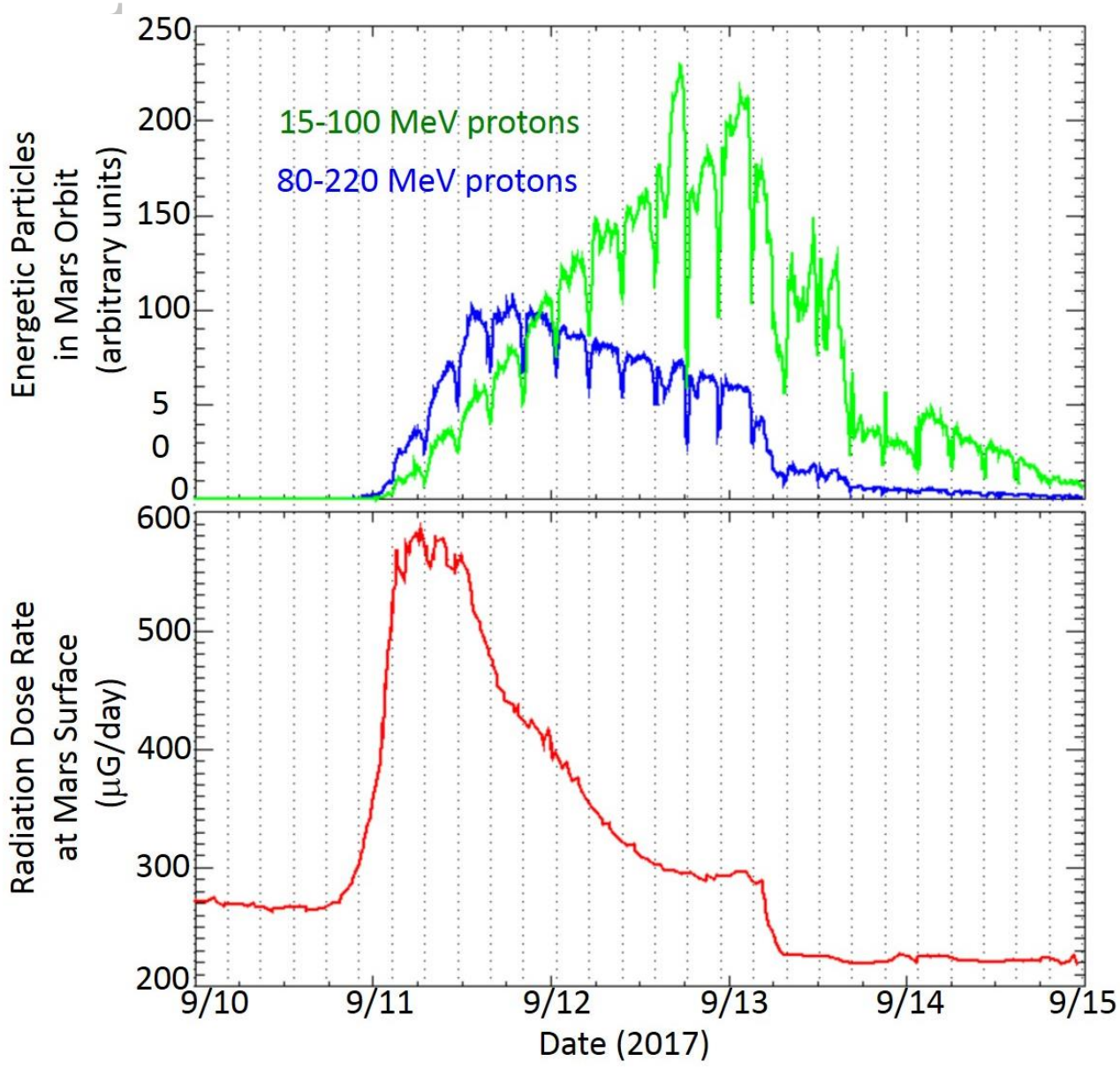

Figure 22. Upper panel: Energetic particles in Mars orbit as measured by MAVEN. Lower panel: Radiation Dose Rate at Mars surface as measured by the MSL-RAD E detector.